Thermobaric flow

A. KAY*

Department of Mathematical Sciences, Loughborough University, Loughborough, Leicestershire, LE11 3TU

Abstract

Simple model flows demonstrating the combined effect of thermobaricity with either salinity variations or nonlinear temperature-dependence in the equation of state of water are investigated. An inviscid flow exhibits a three-layer behaviour, resulting in the formation of a mid-depth temperature maximum, such as is observed in some high-latitude oceans and deep lakes. This may be subsequently overtaken by nonlinear frontogenesis, which in the viscous case is shown to generate a thermal bar. Thermobaricity shifts the thermal bar towards the colder water, and initially produces a slope in the downwelling plume, but this transient feature disappears as the dominant frontogenesis tilts the plume back to the vertical.

Keywords: Baroclinic flow; Frontogenesis; Polar oceans; Thermobaricity

*Fax: +44 1509 223969; Email: A.Kay@Lboro.ac.uk

1 Introduction

The equation of state of water has three features of great importance to the dynamics of deep lakes and oceans: nonlinear temperature-dependence, thermobaricity and salinity-dependence. The nonlinear dependence of density on temperature is such that at atmospheric pressure and zero salinity there is a maximum of density at 3.98°C. Hence a mixture of two waters at different temperatures may be denser than both the original components; this phenomenon is known as cabbeling. Cabbeling results in the thermal bar phenomenon, discovered by Forel (1880), in temperate lakes. Even at oceanic salinities, where the temperature-density relationship is monotonic, cabbeling can still occur if there are variations of salinity as well as temperature: Garrett & Horne (1978) have discussed the role of cabbeling in oceanic fronts and Foster (1972) has shown that an instability due to cabbeling may be important in the formation of Antarctic bottom water.

The variation of the thermal expansion coefficient with pressure, known as thermobaricity (McDougall, 1987), has recently received considerable attention in studies of convection in lakes and oceans (Akitomo, 1999, and references therein). Because of thermobaricity the temperature of maximum density θ_{md} in fresh water decreases with depth at a rate of $0.002°\mathrm{C.m}^{-1}$. This allows the formation of a mid-depth temperature maximum in Winter if the deep waters are warmer than the local value of θ_{md} but cooler than its surface value, and have stable stratification (temperature decreasing with depth): during the Autumn cooling period, these deep waters are not disturbed while convective mixing takes place in a surface layer above 3.98°C, and they still retain their temperature profile while the surface layer is cooled below 3.98°C and develops reverse stratification (temperature increasing with depth)

(Shimaraev & Granin, 1991). However, Carmack & Weiss (1991) have also identified a dynamical process resulting from thermobaricity that could in principle create a mid-depth temperature maximum: this thermobaric flow is illustrated in figure 1. When salinity variations are also present, Aagaard et al. (1985) have shown how a similar process may be responsible for the intrusion of a layer of warm salty water at mid-depth in the Fram Strait.

We present below some mathematical models which elucidate the dynamics of thermobaric flow. In Section 2 we use formalisms developed by Simpson & Linden (1989) and Kay (1992) for the study of frontogenesis in buoyancy-driven flows to solve the dynamical equations for 2-dimensional inviscid flow, using Farmer & Carmack's (1981) freshwater equation of state which incorporates both nonlinearity and thermobaricity in the simplest possible form. As an initial condition we consider a body of water with a uniform horizontal temperature gradient rather than the discontinuity in temperature shown in figure 1. In the non-rotating case the mid-depth temperature maximum forms initially but is overtaken by frontogenesis, resulting from a positive feedback mechanism between steepening density gradients and intensifying convergent flow (Simpson & Linden, 1989; Kay, 1992). Alternatively, if the coriolis force due to planetary rotation is included, there may be a geostrophic adjustment to a steady state if the Rossby number is small enough (Ou, 1984). However, there is no damping to cause an inviscid flow to settle down in its geostrophic equilibrium state, so a strictly inviscid model should exhibit inertial oscillations whose amplitude will grow by the frontogenesis mechanism described above (Blumen, 2000). We consider only the non-rotating case here, but will develop the theory of rotating thermobaric flow in a subsequent paper.

Although nonlinearity of the temperature-density relationship plays a major role in the inviscid model, there is no cabbeling since there is no mixing. By including viscosity and heat conduction in the equations we can model the formation of a thermobaric thermal bar; although there are now numerous thermal bar models in the literature, very few have included the decrease of temperature of maximum density with depth. Among those that have, Tsvetova (1995) and Botte & Kay (2000) have modelled the circulation in a cross-section of Lake Baikal during Spring warming, while S.J. Walker (unpublished manuscript) has made a more fundamental study of the dynamics: Walker's model has initial conditions of horizontal uniformity of temperature below 300 metres depth, whereas in the upper 300 metres there is a vertical discontinuity between regions above and below the temperature of maximum density, temperature profiles being arranged so that densities are equal across the discontinuity at all depths. As mixing starts, the discontinuity becomes a thermal bar with a downwelling plume, which eventually penetrates below 300 metres. A curious feature is that the most rapidly descending water is at a temperature of around 3.8°C, and this appears to undercut cooler denser water; the explanation is that the warmer water has descended from near the surface, so has gathered greater inertia than the cooler water.

In Section 3 of this paper we present a model of viscous thermobaric flow which differs from Walker's model in its initial conditions: consistently with our inviscid model, we start with a simple linear horizontal temperature variation. Evidence of the formation of a mid-depth temperature maximum will be sought, and we shall also examine the effect of thermobaricity on the development of a thermal bar, using a comparison with a model in which thermobaricity is excluded from the equation of

state.

Finally, in section 4 we model the oceanic thermobaric flow of Aagaard *et al.* (1985). The prerequisite for thermobaric flow is that waters of different temperatures should have the same density at some depth, known as the compensation depth h_c. In fresh water it is the nonlinearity of the equation of state that allows this condition to be realised; in seawater it may be realised if salinity varies as well as temperature. Thus we shall concentrate on a simple model of this flow, in which density depends linearly on both temperature and salinity; however, we shall also briefly consider the effects of nonlinearity in the temperature dependence in oceanic flow.

As in some of the other theoretical studies referenced above, the initial conditions for all our models are somewhat artificial. The models are intended to provide some insight into dynamical processes that may be responsible for observed features; even with quasi-stationary features such as the warm, salty intrusion observed by Aagaard *et al.* (1985), there are questions about their origin that can best be investigated by time-dependent analyses starting from simple notional initial conditions.

2 A model of inviscid thermobaric flow in fresh water

2.1 Formulation of the model

We consider two-dimensional flow in a channel of uniform depth h and infinite horizontal extent. The flow is driven by pressure gradients arising from horizontal density variations. We describe the flow in the x-z plane (where x and z are horizontal and

vertical coordinates, respectively, with $z = 0$ at the upper surface of the channel) in terms of the vorticity

$$\omega \equiv \frac{\partial u}{\partial z} - \frac{\partial w}{\partial x} \tag{2.1}$$

where (u, w) are the velocity components in the (x, z) directions. Under the Boussinesq approximation, the vorticity equation is

$$\frac{\partial \omega}{\partial t} = -u\frac{\partial \omega}{\partial x} - w\frac{\partial \omega}{\partial z} + \frac{g}{\rho_m}\frac{\partial \rho}{\partial x}. \tag{2.2}$$

Here ρ is density and ρ_m is a constant reference density, which we take to be the maximum density of water at atmospheric pressure and zero salinity.

The density is given as a function of temperature, pressure and salinity by an equation of state. While precise equations of state are available for both fresh water and sea water (Chen & Millero, 1986; UNESCO, 1981), it is more profitable to use a simple approximation containing the important features of nonlinearity and thermobaricity when seeking to gain insight into the fundamental processes. Such an approximate equation is given by Farmer & Carmack (1981): for water at zero salinity,

$$\rho = \rho_m[1 + p(C_0 - \gamma(\theta - \theta_m)) - \beta(\theta - \theta_m)^2] \tag{2.3}$$

where p is pressure above atmospheric, θ is temperature in degrees Celsius and $\theta_m = 3.98°\mathrm{C}$, the temperature of maximum density for fresh water at atmospheric pressure. The remaining constants in (2.3) have the values

$$\begin{aligned} \rho_m &= 999.975 \text{ kg.m}^{-3} \\ C_0 &= 4.9388 \times 10^{-10} \text{ Pa}^{-1} \\ \gamma &= 3.3039 \times 10^{-12} \text{ °C}^{-1}.\text{Pa}^{-1} \end{aligned}$$

$$\beta \;=\; 8.2545 \times 10^{-6}\ ^{\circ}\mathrm{C}^{-2}.$$

For use in (2.3), pressure may be calculated hydrostatically using the reference density:

$$p = -\rho_m g z; \tag{2.4}$$

this incurs errors of order $p\gamma(\theta - \theta_m)$ (around 10^{-4} for typical conditions in a deep lake such as Baikal) relative to the magnitudes of the terms producing density variations in (2.3). We do not distinguish between *in situ* and potential density and temperature; the difference is rather small, even in the deepest lakes (Farmer, 1975), and introducing adiabatic warming and cooling would unnecessarily complicate the equations. Thus the temperature is simply an advected tracer,

$$\frac{\partial \theta}{\partial t} = -u\frac{\partial \theta}{\partial x} - w\frac{\partial \theta}{\partial z}, \tag{2.5}$$

and the gradient Richardson number may be calculated as

$$\mathrm{Ri} = \frac{-\frac{g}{\rho_m}\frac{\partial \rho}{\partial \theta}\frac{\partial \theta}{\partial z}}{\left(\frac{\partial u}{\partial z}\right)^2}, \tag{2.6}$$

with a value of Ri greater than $\frac{1}{4}$ implying that the flow is stable.

Although the equation of state implies a degree of compressibility, we apply the anelastic approximation whereby the divergence of the velocity vector is zero, so that

$$\frac{\partial u}{\partial x} + \frac{\partial w}{\partial z} = 0. \tag{2.7}$$

When combined with the condition of zero flow across horizontal boundaries, i.e.

$$w = 0 \quad \text{at} \quad z = 0 \quad \text{and at} \quad z = -h, \tag{2.8}$$

this yields

$$\int_{-h}^{0} u\, dz = \text{constant} \tag{2.9}$$

and in the absence of coriolis force it is reasonable to assume that the constant will be zero.

We consider the development of the flow from rest with an initially uniform horizontal temperature gradient λ, i.e.

$$\theta = \theta_m + \lambda x \quad \text{at} \quad t = 0. \tag{2.10}$$

With the equation of state (2.3), this results in an initial density field as illustrated in figure 2. The density of water is at a maximum (with respect to temperature and horizontal position) at $x = 0$ at the surface ($z = 0$). However, the temperature of maximum density decreases with depth at a rate $-\rho_m g\gamma/2\beta$ (from (2.3) and (2.4)), so that at the bed ($z = -h$) water of maximum density is found at $x = -x_\theta$, where

$$x_\theta = \rho_m g\gamma h/2\beta\lambda. \tag{2.11}$$

Note that x_θ is a horizontal length scale for the problem – no such scale exists in the absence of thermobaricity (Kay, 1992).

Two methods of analysis will be used. Firstly, we can obtain useful insight into the early development of the flow in response to buoyancy and inertia forces by obtaining expansions of the form

$$\omega = \omega_0 + \omega_1 t + \omega_2 t^2 + \ldots, \tag{2.12}$$

which are valid at times soon after the start of the flow (Simpson & Linden, 1989). The successive terms in (2.12) and in similar expansions for u, v, w, θ and ρ are obtained by substituting the expansions into the dynamical equations and extracting terms at each order in t. Secondly, we examine the process of frontogenesis by obtaining a full solution to the dynamical equations by the method of characteristsics (Kay, 1992; Grundy & Kay, 2001).

2.2 Early development of the flow: the mid-depth temperature maximum

With the initial density gradient calculated from (2.3) and (2.10), substitutions of the form (2.12) into the vorticity equation (2.2) yield

$$\omega_1 = -Ax + Bz \tag{2.13}$$

at zero'th order in t, where

$$A = 2\beta\lambda^2 g \quad \text{and} \quad B = \gamma\lambda g^2 \rho_m; \tag{2.14}$$

the parameters A and B can be considered as representative of the magnitudes of nonlinear and thermobaric effects, respectively. Note that these parameters are also related to our length scales:

$$\frac{x_\theta}{h} = \frac{B}{A}\,. \tag{2.15}$$

Using (2.1) and (2.7) – (2.9) to obtain the $O(t)$ velocity components from the vorticity (2.13), we find

$$u_1 = -Ax\left(z + \frac{h}{2}\right) + \frac{B}{2}\left(z^2 - \frac{h^2}{3}\right) \tag{2.16}$$

$$w_1 = \frac{A}{2} z(z+h). \tag{2.17}$$

The vertical flow is a consequence of the horizontal convergence which results from nonlinearity in the density profile (Kay, 1992), and is unaffected by thermobaricity. The horizontal component shows a thermobaric term, which introduces a curvature into the profiles of the convergent/divergent flow. Some profiles are shown in figure 3 for locations in the region $-x_\theta \leq x \leq 0$ (i.e. where the density maximum can

be found at some level within the channel): the three-layer flow suggested in figure 1, with warm water collapsing into the mid-depth region of the channel and flowing between layers of cooler water, is seen to occur in the region

$$-\frac{2x_\theta}{3} < x < -\frac{x_\theta}{3}. \tag{2.18}$$

More precisely, the region (2.18) is where the flow at both the upper and lower surfaces of the channel is in the opposite direction to that at some intermediate depth; however, the horizontal velocity has an extremum (with respect to depth) within the channel throughout the region

$$-x_\theta < x < 0. \tag{2.19}$$

Figure 3 also shows that the surface convergence front is initially located at $x = -\frac{1}{3}x_\theta$, as is seen more clearly in a streamline plot (figure 4). Thus thermobaricity causes the convergence front and the downwelling plume to be distinct from the line of maximum density (see figure 2); the plume and the maximum-density line would coincide and be vertical if thermobaric effects were ignored.

The streamline plot obscures the extremum of the horizontal velocity component. Nevertheless, the effect of this extremum in producing a mid-depth temperature maximum may be easily confirmed: from (2.5), the lowest-order perturbation to the initial temperature is

$$\theta_2 = -\frac{\lambda}{2}u_1 = \frac{\lambda}{2}\left\{Ax\left(z + \frac{h}{2}\right) - \frac{B}{2}\left(z^2 - \frac{h^2}{3}\right)\right\} \tag{2.20}$$

which has a maximum with respect to depth at $z = Ax/B$, i.e. located coincident with the original density maximum and the horizontal velocity extremum. From (2.20), profiles of θ_2 have the same form as those of u_1 but with the sign reversed,

so that figure 3 can be seen as a set of profiles of the negative of the temperature perturbation; an isotherm plot (figure 5) shows the mid-depth temperature maximum even more clearly. Finally, since

$$\frac{\partial u}{\partial z} \approx \frac{\partial u_1}{\partial z} t = \frac{g}{\rho_m} \frac{\partial \rho}{\partial \theta} \lambda \tag{2.21}$$

and

$$\frac{\partial \theta}{\partial z} \approx \frac{\partial \theta_2}{\partial z}\, t^2 = -\frac{\lambda}{2} \frac{\partial u_1}{\partial z}, \tag{2.22}$$

we find from (2.6) that $\mathrm{Ri} \approx \frac{1}{2}$, indicating that the flow is stable in this initial stage (cf. Tandon & Garrett, 1994).

Higher-order terms in the expansions are available, but they only provide useful information on the effects of nonlinearity: they show the frontogenesis process as found by Kay (1992), and do not indicate clearly the effects of thermobaricity on this process.

2.3 Thermobaric effects on frontogenesis

The procedure for finding the full solutions to the dynamical equations is only a little more complicated than in the non-thermobaric case (Kay, 1992). Equations (2.10), (2.13), (2.16), (2.17) and (2.20) suggest seeking solutions of the form

$$\theta = \theta_m + Ax\theta_n(z,t) + B\theta_t(z,t) \tag{2.23}$$

$$\omega = Ax\omega_n(z,t) + B\omega_t(z,t) \tag{2.24}$$

$$u = Axu_n(z,t) + Bu_t(z,t) \tag{2.25}$$

$$w = Aw_n(z,t) \tag{2.26}$$

with subscripts n and t referring to nonlinear and thermobaric effects, respectively. We define dimensionless variables by

$$Z = \frac{z+h}{h} \tag{2.27}$$

$$X = \frac{x}{x_\theta} \tag{2.28}$$

$$T = (Ah)^{1/2}t \tag{2.29}$$

$$\Theta_n = \frac{A}{\lambda}\theta_n \tag{2.30}$$

$$\Theta_t = \frac{A}{\lambda h}\theta_t \tag{2.31}$$

$$\Omega_n = (Ah)^{1/2}\omega_n \tag{2.32}$$

$$\Omega_t = \left(\frac{A}{h}\right)^{1/2}\omega_t \tag{2.33}$$

$$U_n = \left(\frac{A}{h}\right)^{1/2}u_n \tag{2.34}$$

$$U_t = \left(\frac{A}{h^3}\right)^{1/2}u_t \tag{2.35}$$

$$W_n = \left(\frac{A}{h^3}\right)^{1/2}w_n \tag{2.36}$$

and substitute (2.23) – (2.36) and the equation of state into the vorticity equation (2.2) and the temperature equation (2.5). After separating terms proportional to x from those independent of x, this yields the following set of first-order quasi-linear partial differential equations:

$$\frac{\partial\Omega_n}{\partial T} = -U_n\Omega_n - W_n\frac{\partial\Omega_n}{\partial Z} - \Theta_n^2 \tag{2.37}$$

$$\frac{\partial\Omega_t}{\partial T} = -U_t\Omega_n - W_n\frac{\partial\Omega_t}{\partial Z} + Z\Theta_n - \Theta_n\Theta_t \tag{2.38}$$

$$\frac{\partial \Theta_n}{\partial T} = -U_n \Theta_n - W_n \frac{\partial \Theta_n}{\partial Z} \tag{2.39}$$

$$\frac{\partial \Theta_t}{\partial T} = -U_t \Theta_n - W_n \frac{\partial \Theta_t}{\partial Z} \,. \tag{2.40}$$

The definition of vorticity (2.1) and the continuity equation yield

$$\Omega_n = \frac{\partial U_n}{\partial Z} = -\frac{\partial^2 W_n}{\partial Z^2} \tag{2.41}$$

$$\Omega_t = \frac{\partial U_t}{\partial Z} \,. \tag{2.42}$$

Initial conditions are

$$\Omega_n = \Omega_t = 0, \quad \Theta_n = 1, \quad \Theta_t = 0 \quad \text{at} \quad t = 0 \tag{2.43}$$

and boundary conditions are

$$W_n = 0 \quad \text{at} \quad Z = 0 \quad \text{and at} \quad Z = 1. \tag{2.44}$$

The formula (2.6) for Richardson number becomes

$$\mathrm{Ri} = \frac{(X\Theta_n + \Theta_t + 1 - Z)\left(X\frac{\partial \Theta_n}{\partial Z} + \frac{\partial \Theta_t}{\partial Z}\right)}{\left(X\frac{\partial U_n}{\partial Z} + \frac{\partial U_t}{\partial Z}\right)^2} \,. \tag{2.45}$$

The solution of (2.37) – (2.40) in terms of characteristics is

$$dT = \frac{dZ}{W_n} = -\frac{d\Omega_n}{U_n\Omega_n + \Theta_n^2} = -\frac{d\Omega_t}{U_t\Omega_n - Z\Theta_n + \Theta_n\Theta_t} = -\frac{d\Theta_n}{U_n\Theta_n} = -\frac{d\Theta_t}{U_t\Theta_n}, \tag{2.46}$$

which may be numerically integrated by a procedure described by Grundy & Kay (2001). Streamline and isotherm plots derived from these numerical integrations were presented for dimensionless time $T = 1.0$ in figures 4 and 5 above, and are now shown for $T = 2.0$ in figures 6 and 7. Temperature gradients near the surface have clearly steepened at $T = 2.0$; the absence of a temperature front at a particular

location is due to the horizontally infinite domain in this model, but we take the steepening of gradients as indicative of frontogenesis. The circulation has moved the surface signature of the line of maximum density a substantial distance to the left, while the surface convergence line has moved a little to the right because it is in a region where the density gradient is creating clockwise vorticity. The mid-depth temperature maximum has been pushed towards the bed by the downwelling flow; its horizontal extent, being the same as that of the line of maximum density, now stretches further to the left due to the divergent flow near the bed.

An isoline plot of Richardson number is shown in figure 8. As the convergent flow near the surface intensifies, its shear increases more rapidly than the stable stratification, so the Richardson number decreases here; as time proceeds, isolines with decreasing values of Ri appear at the surface and then descend. At the same time, the shear of the divergent flow near the bed weakens (relative to the stratification), so that the Richardson number increases here. There is also a region in the vicinity of the mid-depth temperature maximum and the line of maximum density where Ri has wide fluctuations over small distances, and falls to zero at the temperature maximum; values of Ri are not a reliable indicator of stability here, firstly because the simplified formulation of stratification (see caption of figure 2) gives misleading values of Ri in this region, and secondly because the flow has a substantial vertical component here.

The isoline Ri=0.25 appears at the surface at dimensionless time $T = 2.07$. Subsequently the flow near the surface may be destabilised by the shear, resulting in turbulent mixing which will tend to inhibit further frontogenesis. Nevertheless, we have continued to integrate the model equations ignoring the possible instability, in order to compare results with those of Grundy & Kay (2001) for a non-thermobaric

flow. Our equations (2.37), (2.39) and (2.41) are identical to Grundy & Kay's equations, while equations (2.38), (2.40) and (2.42) govern thermobaric effects. Grundy & Kay's solution developed a singularity at the upper surface $Z = 1$ at a dimensionless time $T_b = 2.278235$, so this "finite-time blow-up" will also occur in the present case, but with velocity and temperature profiles on the approach to blow-up altered by thermobaricity.

Figures 9 and 10 show streamlines and isotherms shortly before blow-up. The downwelling plume is now vertical and coincides with the line of maximum density which is also vertical in the upper part of the channel; these features, which would constitute a thermal bar in a channel of finite horizontal extent and with viscosity and heat transfer accounted for, are located at $x \approx -0.27426 x_\theta$ at blow-up. The form of this thermal bar is similar to that in a non-thermobaric model, indicating that thermobaric effects are swamped by frontogenesis as blow-up approaches; however its location is determined by the effects of thermobaricity at earlier times.

In the lower part of the channel the effects of blow-up are felt less strongly, and the thermobaric flow features (extrema of temperature and horizontal velocity component) persist here, being found at a depth of $0.8h - 0.9h$ over a broad region to the left (i.e. cold-water side) of the thermal bar. With regard to blow-up, the temperature maximum can be regarded as irrelevant as $T \to T_b$, since temperature variations in the lower part of the channel are $O(1)$ whereas they are $O((T_b - T)^{-1})$ near the surface; however, the persistence of the temperature maximum in this solution may imply that thermobaric flow is genuinely a possible cause of such phenomena in oceans and deep lakes, and that the temperature maximum should occur near the base of a layer in which thermobaric flow is operating.

The computational results are supported by asymptotic analysis, extending the work of Grundy & Kay (2001) to examine the behaviour of the thermobaric variables on the approach to blow-up. Writing the dimensionless time remaining until blow-up as

$$\tau = T_b - T, \tag{2.47}$$

we obtain the formulae

$$U_t \sim -\frac{C_1}{2\tau \ln \tau}\left[1 + \frac{f(\tau)}{-\ln \tau} + \tau^{-(Z^2-1)} \ln \tau \left\{ Z^2 e^{2b(Z^2-1)} + O\left(\frac{-1}{\ln \tau}\right)\right\}\right], \tag{2.48}$$

$$\Theta_t \sim \tau^{-Z^2}\left[\sqrt{2} C_1 Z e^{2b(Z^2-1)} + O\left(\frac{-1}{\ln \tau}\right)\right], \tag{2.49}$$

which are uniformly valid for $0 < Z \leq 1$ as $\tau \downarrow 0$. In these formulae, $f(\tau)$ is some function (as yet undetermined) which is $O(1)$ as $\tau \downarrow 0$; b is a coefficient which arises in the solution of the nonlinear equations (Grundy & Kay, 2001), being determined by initial conditions and estimated from computations to have a value of about -0.16; C_1 is a constant of proportionality arising because we are solving linear equations (2.38) and (2.40) for the thermobaric variables, and so can only be determined by computation from the initial conditions.

The final two terms in (2.38), which characterise the thermobaric effect, do not affect the asymptotic analysis to the order given in (2.48) and (2.49); the thermobaric variables are simply driven to blow-up by the nonlinear variables, but the specifically thermobaric behaviour is swamped by the nonlinear effects at this stage of the flow. Thus the formulae (2.48) and (2.49) have similar forms to Grundy & Kay's formulae for the nonlinear variables; combining these results according to (2.23) and (2.25), we

find that

$$u \sim -\frac{(Ah)^{1/2}}{2\tau \ln \tau}\left(1 + Z^2 e^{2b(Z^2-1)}\tau^{-(Z^2-1)} \ln \tau\right)(x + C_1 x_\theta) \tag{2.50}$$

$$\theta - \theta_m \sim \sqrt{2}\lambda z e^{2b(Z^2-1)}\tau^{-Z^2}(x + C_1 x_\theta), \tag{2.51}$$

so that u and θ must remain small at $x = -C_1 x_\theta$ as $\tau \downarrow 0$, while the values of these quantities become unbounded at other horizontal stations for all Z (except possibly in a layer of dimensionless thickness of order $(-\ln \tau)^{-1/2}$ at the bed, see Grundy & Kay, 2001). From (2.51) the location $x = -C_1 x_\theta$ is the line of maximum density, so we identify $C_1 \approx 0.27426$ from the computational results.

3 Thermal bar development in viscous thermobaric flow

3.1 Formulation of the mathematical model

We now develop a two-dimensional thermobaric flow model including viscosity and heat conduction. We consider the flow in a rectangular cavity $0 \le x \le L, -h \le z \le 0$, with small aspect ratio (all calculations presented below are for $L = 15\,\mathrm{km}, h = 750\,\mathrm{m}$, but similar results have been obtained with different aspect ratios); this is in contrast to the horizontally unbounded domain of our inviscid model, and will ensure that frontogenesis is localised. For spatially uniform eddy viscosities ν_x and ν_z in the horizontal and vertical directions respectively, the vorticity equation is

$$\frac{\partial \omega}{\partial t} = -u\frac{\partial \omega}{\partial x} - w\frac{\partial \omega}{\partial z} + \frac{g}{\rho_m}\frac{\partial \rho}{\partial x} + \nu_x \frac{\partial^2 \omega}{\partial x^2} + \nu_z \frac{\partial^2 \omega}{\partial z^2}, \tag{3.1}$$

while the temperature equation is

$$\frac{\partial \theta}{\partial t} = -u\frac{\partial \theta}{\partial x} - w\frac{\partial \theta}{\partial z} + K_x\frac{\partial^2 \theta}{\partial x^2} + K_z\frac{\partial^2 \theta}{\partial z^2}, \tag{3.2}$$

where eddy diffusivities of heat K_x and K_z are again assumed spatially uniform. To satisfy the zero-divergence condition (2.7) we introduce a stream function ψ by

$$u = -\frac{\partial \psi}{\partial z}, \qquad w = \frac{\partial \psi}{\partial x}, \tag{3.3}$$

so that

$$\nabla^2 \psi = -\omega. \tag{3.4}$$

The vertical sides and the base of the cavity are rigid, no-slip, insulating boundaries. The upper surface is considered a free surface in the sense of having zero stress (we do not include wind forcing in the model), but displacements of this surface are ignored. We also impose zero heat flux on this surface; this is in contrast to the majority of thermal bar models which are driven by surface heating, but is appropriate to our aim of examining the mechanics of thermobaric flow and frontogenesis. These boundary conditions are expressed as

$$\psi = 0 \qquad \text{on} \qquad x = 0,\ x = L,\ z = -h,\ z = 0; \tag{3.5}$$

$$\frac{\partial \psi}{\partial n} = 0 \qquad \text{on} \qquad x = 0,\ x = L,\ z = -h; \qquad \frac{\partial^2 \psi}{\partial n^2} = 0 \quad \text{on} \quad z = 0; \tag{3.6}$$

$$\frac{\partial \theta}{\partial n} = 0 \qquad \text{on} \qquad x = 0,\ x = L,\ z = -h,\ z = 0. \tag{3.7}$$

Here $\partial/\partial n$ represents the derivative normal to a boundary.

Initial conditions are similar to those in the inviscid model, with the fluid at rest with a linear horizontal temperature variation and no stratification. In the calcula-

tions presented below, we have taken the initial temperature distribution to be

$$\theta_0 = \left(\frac{x}{L} + 0.35\right)\theta_m, \tag{3.8}$$

giving a range of temperatures from approximately 1.4°C to 5.4°C from left to right across the domain; water of maximum density (for the appropriate pressure) is found at $x = 0.65L$ at the surface and at about $x = 0.275L$ at the bed. Having a broad region in which water of maximum density is found at some depth should make thermobaric effects clear, but there is the disadvantage that end-wall effects may be too prominent.

For the purposes of numerical solution, we use dimensionless variables defined as follows (differently from the inviscid calculations):

$$\xi = \frac{x}{L} \tag{3.9}$$

$$\zeta = \frac{z}{L} \tag{3.10}$$

$$\Theta = \frac{\theta - \theta_m}{\theta_m} \tag{3.11}$$

$$\tau = \left(\frac{g\beta\theta_m^2}{L}\right)^{1/2} t \tag{3.12}$$

$$\Psi = \left(g\beta\theta_m^2 L^3\right)^{-1/2} \psi \tag{3.13}$$

$$U = \left(g\beta\theta_m^2 L\right)^{-1/2} u \tag{3.14}$$

$$W = \left(g\beta\theta_m^2 L\right)^{-1/2} w \tag{3.15}$$

$$\Omega = \left(\frac{g\beta\theta_m^2}{L}\right)^{-1/2} \omega. \tag{3.16}$$

The vorticity and temperature equations can then be written

$$\frac{\partial \Omega}{\partial \tau} = \frac{\partial(\Omega, \Psi)}{\partial(\xi, \zeta)} - (2\Theta - \epsilon\zeta)\frac{\partial \Theta}{\partial \xi} + \mathrm{Gr}_x^{-1/2}\frac{\partial^2 \Omega}{\partial \xi^2} + \mathrm{Gr}_z^{-1/2}\frac{\partial^2 \Omega}{\partial \zeta^2} \tag{3.17}$$

$$\frac{\partial \Theta}{\partial \tau} = \frac{\partial(\Theta, \Psi)}{\partial(\xi, \zeta)} + \mathrm{Gr}_x^{-1/2}\mathrm{Pr}_x^{-1}\frac{\partial^2 \Theta}{\partial \xi^2} + \mathrm{Gr}_z^{-1/2}\mathrm{Pr}_z^{-1}\frac{\partial^2 \Theta}{\partial \zeta^2}, \tag{3.18}$$

and (3.4) becomes

$$\nabla^2 \Psi = -\Omega. \tag{3.19}$$

Here the horizontal and vertical Grashof numbers are defined by

$$\mathrm{Gr}_{x,z} = \frac{g\beta\theta_m^2 L^3}{\nu_{x,z}^2} \tag{3.20}$$

and the Prandtl numbers are

$$\mathrm{Pr}_{x,z} = \frac{\nu_{x,z}}{K_{x,z}}. \tag{3.21}$$

The equation of state (2.3), with pressure given by (2.4), has been incorporated into (3.17), and we have introduced the "thermobaricity parameter"

$$\epsilon = \frac{g\rho_m \gamma L}{\beta\theta_m} \tag{3.22}$$

which has the value 14.8 for the data given above. We have set $Gr_x = 10^8$ and $Gr_z = 10^{10}$, corresponding to eddy viscosities $\nu_x \approx 7\,\mathrm{m}^2.\mathrm{s}^{-1}$ and $\nu_z \approx 0.7\,\mathrm{m}^2.\mathrm{s}^{-1}$, in the calculations described below. These rather large viscosities were chosen mainly to ensure stability of the computations; experiments with more realistic values showed the flow developing in a very similar manner to that shown below (except near the end-walls of our domain), but numerical instabilities prevented these computations from running for as long as desired. Prandtl numbers were set to unity, on the assumption that turbulent processes diffuse heat and vorticity at similiar rates.

The system of equations (3.17) – (3.19) is solved by the finite-difference method, using Arakawa's (1966) representation of the nonlinear advection terms (written as Jacobians in (3.17) and (3.18)), which conserves mean square vorticity and kinetic energy. An integration was done with ϵ set to zero, i.e. with a quadratic temperature-density relation but no thermobaricity, for comparison with the case where the full thermobaric equation of state (2.3) is used.

3.2 Results

Streamlines and isotherms for the thermobaric case are shown in figures 11 and 12 for dimensionless time $\tau = 8.0$ (where one dimensionless time unit is a little less than one hour, according to (3.12) with the given data). There is evidence in figure 12 of a rather weak mid-depth temperature maximum, barely visible as a slight leftward bulge in the isotherms to the left of the $\theta = \theta_m$ isotherm, occurring at greater depth for isotherms at lower temperatures – although towards the bottom left of this figure the curvature of isotherms is due to friction at the bed retarding the flow diverging from below the thermal bar. In contrast, the non-thermobaric case (not shown here) shows even more prominent bulges in isotherms near the bottom left, but no such effect around mid-depth.

At time $\tau = 8.0$ the convergence front has not moved from its initial location at $x \approx 0.525L$ (see figure 11), but the downwelling plume has become more vertical (the dividing streamline would initially meet the bed at $x \approx 0.4L$). The upper part of the line of maximum density also becomes more vertical (figure 12), while its surface signature has migrated substantially towards the convergence front from its initial location at $x = 0.65L$, as in the inviscid case. There is evidence of frontogenesis in

figure 12, with isotherms crowding together around the line of maximum density in the upper half of the domain.

Figures 13 and 14 show the situation at time $\tau = 16.0$, when frontogenesis is complete; the line of maximum density is now aligned with the downwelling plume in the upper half of the domain, and the frontogenetic effect of the convergent flow near the surface is balanced by horizontal diffusion of heat across the front. The front is noticeably asymmetric, with the steep temperature gradient mainly on the warm side of the $\theta = \theta_m$ isotherm. This asymmetry, which is also evident at earlier times (figure 12), is due to the separation of the downwelling plume from the line of maximum density in the early stages of the flow. In the region between these two features, vorticity is being generated in the opposite sense to the large-scale rotation of the fluid. Frontogenesis, characterised by Kay (1992) as a positive feedback process involving the density gradient, the vorticity and the horizontal flow convergence, is thus being inhibited in a region on the cold side of the line of maximum density during the early development of the flow, while it proceeds without hindrance on the warm side. The positive feedback amplifies this difference, which is then evident in the final form of the front. A related effect is that the stratification is very weak (isotherms are nearly vertical) on the cold side of the front, so that the Richardson number here is very low; however, since we have taken large values of eddy viscosities, it can be argued that we have already accounted for the turbulence resulting from any shear instability.

Figures 13 and 14 represent a quasi-steady state, with any subsequent evolution of the flow and temperature distribution being on a much slower time-scale. The thermal bar is migrating slowly to the left, possibly as a result of the asymmetry

described above, and is already further to the left than predicted by the inviscid model; but its form remains essentially unchanged. A temperature maximum does persist below the line of maximum density, but it is not clear to what extent this is due to thermobaric flow or simply to bed friction.

4 Oceanic thermobaric flow

Aagaard *et al.* (1985) have described an oceanic flow of similar form to the freshwater thermobaric flow shown in figure 1. In the Fram Strait the relatively warm and salty Eurasian Basin Deep Water (EBDW) from the Arctic Ocean is observed to intrude into the cooler, fresher Greenland Sea Deep Water (GSDW) at depths of around 1500 m.

To model this flow we adopt a simplified equation of state of the type used by Garwood *et al.* (1994), featuring linear dependence of density on both salinity and temperature, and including a thermobaric term:

$$\rho = \overline{\rho}[1 + p(C - \gamma_s(\theta - \overline{\theta})) - \alpha(\theta - \overline{\theta}) + \sigma(S - \overline{S})], \tag{4.1}$$

where S is salinity in psu (practical salinity units, i.e. parts per thousand), $\overline{\theta}$, $\overline{S}$ and $\overline{\rho}$ are reference values of temperature, salinity and density, respectively. Values of other relevant constants may be found from data in Garwood *et al.* (1994):

$$\begin{aligned} \overline{\rho} &= 1.028 \times 10^3 \text{ kg.m}^{-3} \\ \gamma_s &= 2.83 \times 10^{-12} \text{ °C}^{-1}.\text{Pa}^{-1} \\ \alpha &= 2.75 \times 10^{-5} \text{ °C}^{-1} \end{aligned}$$

$$\sigma \;=\; 7.91 \times 10^{-4}\ \mathrm{psu}^{-1},$$

and the compressibility constant C is not given by Garwood *et al.* and has no effect on the dynamics. The compensation depth, at which waters with temperature and salinity values (θ_1, S_1) and (θ_2, S_2) have the same density, is

$$h_c = \frac{\sigma(S_2 - S_1) - \alpha(\theta_2 - \theta_1)}{\overline{\rho} g \gamma_s (\theta_2 - \theta_1)}. \tag{4.2}$$

With Aagaard *et al.*'s (1985) temperature and salinity data for GSDW and EBDW in the Fram Strait, this yields $h_c \approx 2400$ m.; the discrepancy with Aagaard *et al.*'s calculated value of 1900 m. is due to the approximations made in our equation of state, and is of no importance to our modelling of the flow.

Our model uses the dynamical equations and boundary conditions set out in §2.1 above for inviscid flow, together with an advection equation for salinity,

$$\frac{\partial S}{\partial t} = -u\frac{\partial S}{\partial x} - w\frac{\partial S}{\partial z}, \tag{4.3}$$

and the initial conditions of a body of water at rest with uniform horizontal temperature and salinity gradients, i.e.

$$\theta = \overline{\theta} + \lambda x \qquad \text{and} \qquad S = \overline{S} + \mu x \qquad \text{at} \qquad t = 0. \tag{4.4}$$

In this scenario (4.2) becomes

$$h_c = \frac{\sigma\mu - \alpha\lambda}{\overline{\rho} g \gamma_s \lambda}, \tag{4.5}$$

so that the compensation depth exists within a water body of depth h if

$$\frac{\alpha}{\sigma} < \frac{\mu}{\lambda} < \frac{\alpha}{\sigma} + \frac{\overline{\rho} g \gamma_s h}{\sigma}. \tag{4.6}$$

Irrespective of whether this condition is satisfied, the dynamical equations have an exact solution in which the horizontal flow accelerates from rest at a rate

$$a(z) = \left\{ \overline{\rho} g \gamma_s \lambda \left(\frac{z^2}{2} - \frac{h^2}{6} \right) + (\sigma\mu - \alpha\lambda)(z+h) \right\} g \tag{4.7}$$

and there is no vertical motion, due to the linearity of the equation of state (4.1) and the infinite horizontal extent of the domain. Thus the velocity components at time t are

$$u = a(z)t, \qquad w = 0 \tag{4.8}$$

and the temperature and salinity are

$$\theta = \lambda \left(x - \frac{1}{2} a(z) t^2 \right), \qquad S = \mu \left(x - \frac{1}{2} a(z) t^2 \right), \tag{4.9}$$

while the Richardson number, calculated as

$$\mathrm{Ri} = \frac{-\frac{g}{\rho_m} \left(\frac{\partial \rho}{\partial \theta} \frac{\partial \theta}{\partial z} + \frac{\partial \rho}{\partial S} \frac{\partial S}{\partial z} \right)}{\left(\frac{\partial u}{\partial z} \right)^2}, \tag{4.10}$$

(cf. (2.6)) has the constant value $\frac{1}{2}$, indicating stability at all times. The term in (4.7) that is linear in z arises from the linear dependence of density on temperature and salinity, while the term that is quadratic in z arises from thermobaricity; the presence of this term creates maxima in the vertical profiles of both temperature and salinity at the compensation depth $z = h_c$, arising from a flow in which the horizontal velocity also has an extremum at this depth. These findings are in accord with the reasoning of Aagaard *et al.* (1985), even though these authors considered adjacent bodies of water with a sharp change in temperature and salinity between them, rather than a constant gradient of these properties.

The simplifications in our model lead to the absence of any horizontal variation of the velocity, temperature and salinity profiles and the absence of any vertical motion.

However, vertical motion will occur if we take account of the nonlinear temperature dependence in the equation of state. A simple way to model the effects of nonlinearity is to propose an equation of state of a similar form to the freshwater equation (2.3), but adding linear salinity dependence:

$$\rho = \overline{\rho}[1 + p(C_s - \gamma_s(\theta - \overline{\theta})) - \beta_s(\theta - \overline{\theta})^2 + \alpha(S - \overline{S})]. \tag{4.11}$$

The constants in (4.11) may be obtained by fitting the equation to values of density for temperatures, salinities and pressures within the range of interest, noting that the equation will not be accurate outside these ranges. Using Aagaard *et al.*'s (1985) temperature and salinity values for GSDW and EBDW and for a 1:1 mixture of these waters, all at the compensation pressure for which GSDW and EBDW have the same density, and evaluating densities from the International Equation of State of Seawater (UNESCO, 1981), we obtain $\beta_s \approx 2.8 \times 10^{-6}\ {}^{\circ}\mathrm{C}^{-2}$ and $\overline{\theta} \approx -8{}^{\circ}\mathrm{C}$, taking α and γ_s to have the same values as used in (4.1). The reference temperature $\overline{\theta}$ in (4.11) is a notional temperature of maximum density, which does not explicitly depend on salinity (unlike in Farmer & Carmack's (1981) freshwater equation of state). At constant salinity $S > 24.7\,\mathrm{psu}$ the maximum of density (with respect to temperature) is reached at the freezing point, but it has been recognised since Witte's (1902) seminal account of the cabbeling phenomenon that nonlinearity of the temperature dependence is important in ocean dynamics.

If we again suppose that there are initially uniform horizontal temperature and salinity gradients as given by (4.4), we find with the equation of state (4.11) that there is an initial density maximum (with respect to horizontal position) at

$$x = \frac{\alpha\mu + \overline{\rho}g\gamma_s\lambda z}{2\beta_s\lambda^2}\,, \tag{4.12}$$

i.e. at a position which varies linearly with depth. The initial density structure is in fact identical to that for fresh water, apart from a horizontal shift indicated by the term $\alpha\mu$ in (4.12) (i.e. due to the salinity gradient) and, more importantly, the difference in the value of the coefficient of the quadratic term in the equation of state: β_s as estimated above has a value about one-third that of the freshwater coefficient β. Thus the flow will take the same form as freshwater thermobaric flow, but with slower frontogenesis. The time-scale for frontogenesis is

$$t_f = (2\beta_s \lambda^2 g h)^{-1/2} \tag{4.13}$$

(from (2.29) with (2.14)); for conditions in the Fram Strait, with a temperature difference of 0.33°C over a distance of order 1000 km in water of depth around 3 km (Aagaard et al. 1985), t_f is of order 3 months. The contrast with the time-scale of less than a day found in the model described in §3 above is due mainly to the contrast in temperature gradients: in §3 we considered temperature variations of 4°C over the width of a moderate-sized lake. The slowness of frontogenesis in the oceanic conditions suggests that the model based on the linear equation of state (4.1) may provide an adequate explanation of thermobaric flow effects, in particular the mid-depth temperature and salinity maximum, in polar oceans.

5 Conclusions

We have considered some simple model flows to illustrate the combined effects of three of the distinctive features of the equation of state of water. These are, firstly, thermobaricity, which may be thought of either as an increase in the thermal expansion coefficient with increasing pressure or as a decrease in compressibility with increasing

temperature; secondly, the nonlinearity of the temperature-dependence of density, in particular the existence in fresh water of a temperature of maximum density (decreasing with depth due to thermobaricity); and thirdly, the increase in density with salinity. The initial conditions in our models are greatly simplified: uniform horizontal gradients of temperature and, if applicable, salinity are used to represent any horizontal non-uniformity of these quantities as simply as possible; the absence of any initial motion or stratification allows us to see clearly how the flow and stratification develop in response to the imposed temperature and salinity gradients.

Our inviscid models have confirmed the possibility of three-layer horizontal "thermobaric flows", as speculated by Aagaard *et al.* (1985) and Carmack & Weiss (1991) in polar oceans and deep temperate lakes, respectively. This flow creates a mid-depth temperature maximum, which in fresh water appears in a region where the surface water is colder than its temperature of maximum density. However, it does not necessarily follow that observed mid-depth temperature maxima in lakes and oceans are a result of this mechanism. In particular, the annual cycle of surface heating and cooling provides a much stronger mechanism to create the relatively shallow (around 200 m depth) Winter temperature maximum in Lake Baikal (Shimaraev & Granin, 1991), although thermobaric flow may still have some influence on the temperature profile at deeper levels. In the Fram Strait, on the other hand, the much deeper temperature maximum cannot be explained by surface cooling, and the horizontal thermobaric flow seems a more likely mechanism for the creation of this feature. Furthermore, the nonlinearity of the temperature-dependence, which leads to frontogenesis, is weaker in the polar oceans than in a freshwater lake; thus the mid-depth temperature maximum, which results from a linear phenomenon (the horizontal thermobaric flow),

can remain more prominent in the ocean. In contrast, frontogenesis will occur more rapidly in a lake near the temperature of maximum density, so the mid-depth temperature maximum becomes a relatively weak feature, though it can persist in the lower part of the water body where the flow is divergent rather than frontogenetic.

When frontogenesis occurs, leading to the formation of a thermal bar in fresh water, thermobaricity does nevertheless influence the process. Firstly there are some transient effects: the downwelling plume is initially distinct from the line of maximum density, and both are sloping (this is unrelated to the sloping thermal bars reported in some studies which ignore thermobaricity (e.g. Elliott, 1971), where the slope is due to motion of the thermal bar across a lake surface as the lake is progressively warmed). These features disappear as the thermal bar reaches a quasi-steady state in which the downwelling plume and the line of maximum density are coincident and vertical (as in the absence of thermobaricity). However, there are some lasting effects of thermobaricity: the thermal bar is displaced to the cold side of where the maximum-density surface water would otherwise be found, and the region of steep density gradient is asymmetric about the temperature of maximum density.

Acknowledgements

The author is grateful to Dr. E.C. Carmack for suggesting the study of thermobaric flow and for arranging hospitality at the Institute of Ocean Sciences, Sidney, B.C., during a visit by the author in June 1997, funded by the Royal Society. Anonymous reviewers of an earlier version of this paper provided useful comments, in particular the suggestion to analyse stability of the flows by calculating Richardson number.

References

Aagaard, K., Swift, J.H. and Carmack, E.C., 1985. Thermohaline circulation in the Arctic Mediterranean seas. *J. Geophys. Res.*, **90**: 4833 – 4846.

Akitomo, K., 1999. Open-ocean deep convection due to thermobaricity. 1. Scaling argument. *J. Geophys. Res.*, **104**: 5225 – 5234.

Arakawa, A., 1966. Computational design for long-term numerical integration of the equations of fluid motion: two-dimensional incompressible flow. Part 1. *J. Comput. Phys.*, **1**: 119 – 143.

Blumen, W., 2000. Inertial oscillations and frontogenesis in a zero potential vorticity model. *J. Phys. Oceanogr.*, **30**: 31 – 39.

Botte, V. and Kay, A., 2000. A numerical study of plankton population dynamics in a deep lake during the passage of the Spring thermal bar. *J. Marine Systems*, **26**: 367 –386.

Carmack, E.C. and Weiss, R.F., 1991. Convection in Lake Baikal: an example of thermobaric instability. In: P.C.Chu & J.C.Gascard (Editors), *Deep Convection and Deep Water Formation in the Oceans*. Elsevier Oceanography Series **57**: 215 – 228.

Chen, C.T.A. and Millero, F.J., 1986. Precise thermodynamic properties for natural waters covering only the limnological range. *Limnol. Oceanogr.*, **31**: 657 – 662.

Elliott, G.H., 1971. A mathematical study of the thermal bar. *Proc. 14th Conf. Great Lakes Res.*, pp. 545 – 554.

Farmer, D.M., 1975. Potential temperatures in deep freshwater lakes. *Limnol. Oceanogr.*, **20**: 634 – 635.

Farmer, D.M. and Carmack, E.C., 1981. Wind mixing and restratification in a lake near the temperature of maximum density. *J. Phys. Oceanogr.*, **11**: 1516 – 1533.

Forel, F.A., 1880. La congélation des lacs suisses et savoyards pendant l'hiver 1879-1880. §11. Lac Léman. *L'Écho des Alpes*, **3**: 149 – 161.

Foster, T.D.,. 1972 An analysis of the cabbeling instability in sea water. *J. Phys. Oceanogr.*, **2**: 294 – 301.

Garrett, C. and Horne, E., 1978. Frontal circulation due to cabbeling and double diffusion. *J. Geophys. Res.*, **83**: 4651 – 4656.

Garwood, R.W., Isakari, S.M. and Gallacher, P.C., 1994. Thermobaric convection. In: O. Johannessen, R. Muench and J. Overland (Editors), *The Polar Oceans and their Role in Shaping the Global Environment.* Geophys. Monogr. Ser. **85**: 199 – 209. AGU, Washington D.C..

Gill, A.E., 1982 *Atmosphere-Ocean Dynamics.* Academic Press, London.

Grundy, R.E. and Kay, A., 2001. The asymptotics of blow-up in Boussinesq flow and related systems. Submitted to *IMA J. Appl. Math.*

Kay, A., 1992. Frontogenesis in gravity-driven flows with non-uniform density gradients. *J. Fluid Mech.*, **235**: 529 – 556.

McDougall, T.J., 1987. Thermobaricity, cabbeling and water-mass conversion. *J. Geophys. Res.*, **92**: 5448 – 5664.

Ou, H.W., 1984. Geostrophic adjustment: a mechanism for frontogenesis. *J. Phys. Oceanogr.*, **14**: 994 – 1000.

Peeters, F., Piepke, G., Kipfer, R., Hohmann, R. and Imboden, D.M., 1996. Description of stability and neutrally buoyant transport in freshwater lakes. *Limnol. Oceanogr.*, **41**: 1711 – 1724.

Shimaraev, M.N. and Granin, N.G., 1991. Temperature stratification and the mechanisms of convection in Lake Baikal. *Dokl. Akad. Nauk SSSR*, **321**: 831 – 835. (In

Russian).

Simpson, J.E. and Linden, P.F., 1989. Frontogenesis in a fluid with horizontal density gradients. *J. Fluid Mech.*, **202**: 1 – 16.

Tandon, A. and Garrett, C., 1994. Mixed layer restratification due to a horizontal density gradient. *J. Phys. Oceanogr.*, **24**: 1419 – 1424.

Tsvetova, E.A., 1995. Convective currents associated with the thermal bar of Lake Baikal. In: A.S. Alekseev and N.S. Bakhvalov (Editors), *Advanced Mathematics: Computations and Applications*. NCC Publisher, pp. 386 – 393.

UNESCO, 1981. Tenth report of the joint panel on oceanographic tables and standards. *UNESCO Technical Papers in Marine Science*, **36**.

Witte, E., 1902. Zur Theorie der Stromkabbelungen. *Gaea*, **38**: 484 – 487.

Figure captions

Figure 1: Schema illustrating the mechanism of thermobaric flow for adjacent homogeneous columns of water at different temperatures but equal density at mid-depth (from Carmack & Weiss, 1991). At the surface, water at temperature T_2 is denser than water at T_1 (being closer to the temperature of maximum density $T_{\rho\max}$), but at the bed , water at T_1 is denser: hence the adjustment whereby water at T_1 rises in the upper half of the basin but sinks in the lower half.

Figure 2: The initial density field for the inviscid thermobaric flow model. The contour interval is $0.1\rho_m A x_\theta^2/g$, where A and x_θ are given by (2.13) and (2.10) respectively (contours in the upper left region are closely packed and have been omitted for clarity). See equations (2.27), (2.28) and (2.11) for definitions of the dimensionless coordinates X and Z used here and in figures 3 – 10. The bold line is the locus of maximum density (with respect to horizontal coordinate). Note that the compressibility term pC_0 is ignored in calculating density from (2.3) for this plot; this term would vanish if potential density were calculated. The stability is actually positive or neutral everywhere, despite the appearance of a region of static instability in this plot. This region would not be entirely eliminated by plotting potential density: as explained by Gill (1982), §3.7, and in more detail by Peeters *et al.* (1996), potential density can give misleading indications of stability in cases where the thermal expansion coefficient varies down the water column. Hence we use the simpler formulation of density, noting that it is horizontal density gradients that are fundamental to the dynamics in our model.

Figure 3: Profiles of leading-order horizontal velocity u_1 at early times in the development of inviscid thermobaric flow. The profiles are shown at $x = -x_\theta$, $x = -\frac{2}{3}x_\theta$,

$x = -\frac{1}{2}x_\theta$, $x = -\frac{1}{3}x_\theta$ and $x = 0$. These profiles also represent the negative of the lowest-order temperature perturbation θ_2.

Figure 4: Streamlines, at intervals of 0.01 dimensionless units, at dimensionless time $T = 1.0$ from the numerical solution described in §2.3, but representative of the early development of the flow. Note in particular the dividing streamline, representing a downwelling plume originating at a convergence front on the surface at $x = -\frac{1}{3}x_\theta$.

Figure 5: Isotherms at dimensionless time $T = 1.0$ from the numerical solution described in §2.3, but representative of the early development of the flow. The isotherm interval is 0.1 dimensionless units, and the bold line is the line of maximum density.

Figure 6: Streamlines, at intervals of 0.025 dimensionless units, at dimensionless time $T = 2.0$ in inviscid thermobaric flow. The flow has strengthened since $T = 1.0$ (figure 4) and the dividing streamline is closer to vertical.

Figure 7: Isotherms at dimensionless time $T = 2.0$ in inviscid thermobaric flow, showing steepening (slackening) of temperature gradients near the surface (bed), with the mid-depth temperature maximum shifted towards the bed. Note that this figure shows a broader domain than previous figures. The isotherm interval is 0.2 dimensionless units, and the bold line is the line of maximum density; closely packed isotherms in the upper left and upper right regions have been omitted for clarity.

Figure 8: Isolines of Richardson number, at intervals of 0.05, at dimensionless time $T = 2.0$ in inviscid thermobaric flow. The main feature is the general increase in Ri (and hence of stability) with increasing depth. Isolines are omitted in a region around the mid-depth temperature maximum and the line of maximum density, where Ri varies widely over short distances.

Figure 9: Streamlines, at intervals of 8.0 dimensionless units, at dimensionless time

$T = 2.278$ in inviscid thermobaric flow (with blow-up occuring at $T = 2.278235$). The dividing streamline is now vertical and its surface signature coincides with that of the line of maximum density (see figure 10).

Figure 10: Isotherms at dimensionless time $T = 2.278$ in inviscid thermobaric flow. The impression of a sharp front is misleading: isotherms are only shown for temperatures between -2.0 and 2.0 dimensionless units (at intervals of 0.2 units), and temperature gradients are in fact very steep across the entire near-surface region. In contrast, very slack gradients and a temperature maximum are found near the bed. The bold line is the line of maximum density.

Figure 11: Streamlines for viscous thermobaric flow in a rectangular cavity of length $L = 15$km and depth $h = 750$m, at dimensionless time $\tau = 8.0$. The dividing streamline marks the centre-line of a downwelling plume. See equations (3.9) and (3.10) for definitions of the dimensionless coordinates ξ and ζ used here and in the remaining figures.

Figure 12: Isotherms for viscous thermobaric flow at dimensionless time $\tau = 8.0$. The isotherm interval is $0.1\theta_m$ (about 0.4°C), and the bold line is the contour of maximum density.

Figure 13: As figure 11, but at $\tau = 16.0$.

Figure 14: As figure 12, but at $\tau = 16.0$.

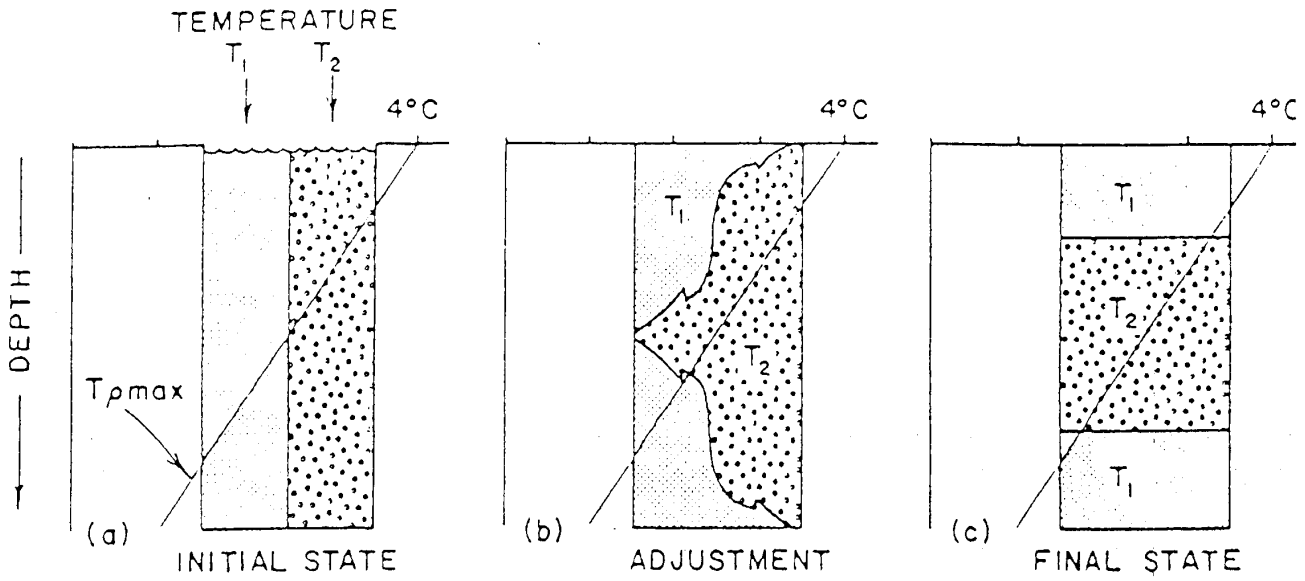
TEMPERATURE
T1
T2
4°C
DEPTH
Tρmax
(a)
INITIAL STATE
4°C
T1
T2
(b)
ADJUSTMENT
4°C
T1
T2
T1
(c)
FINAL STATE

Kay : Figure 1

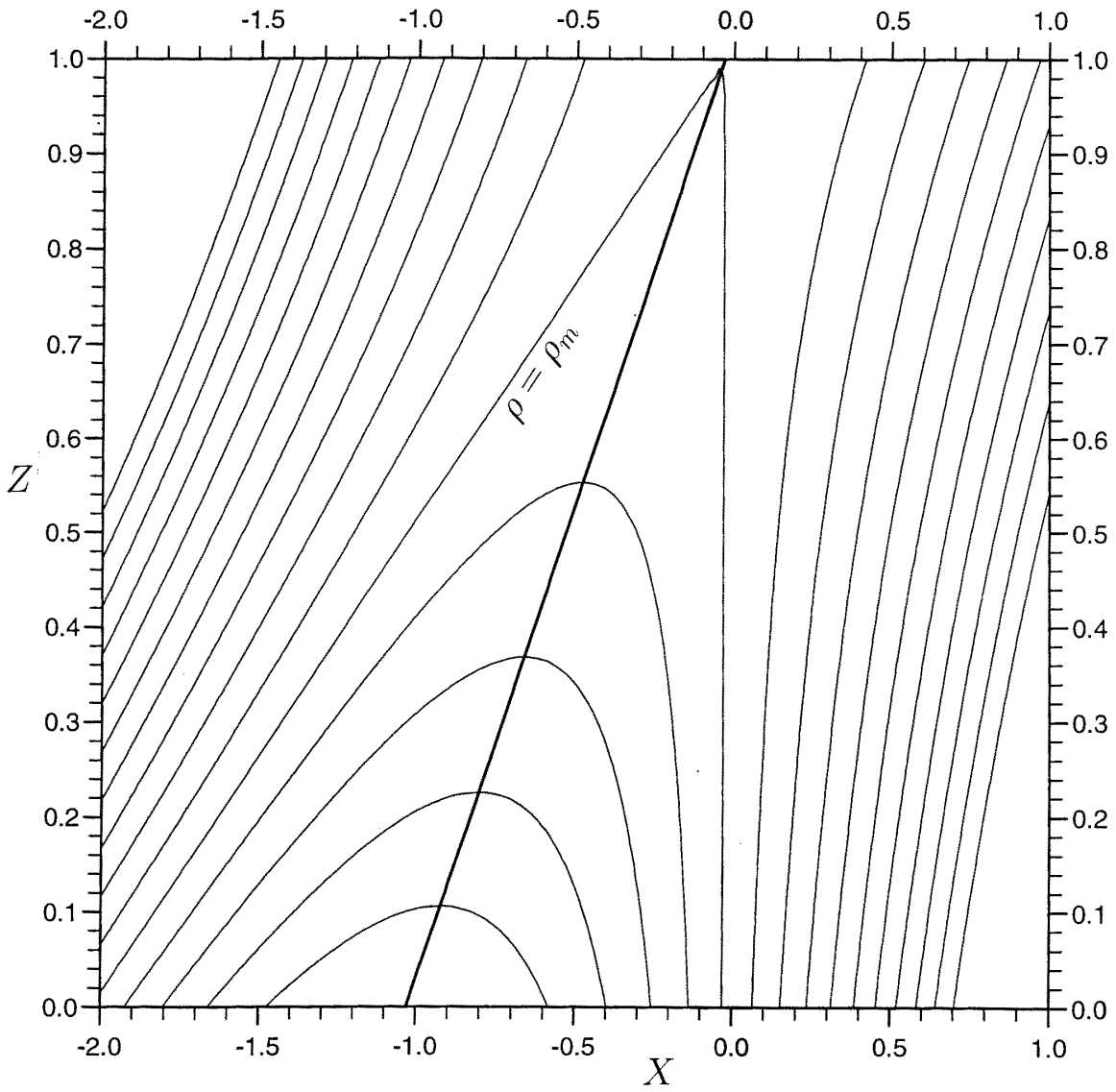

Kay : Figure 2

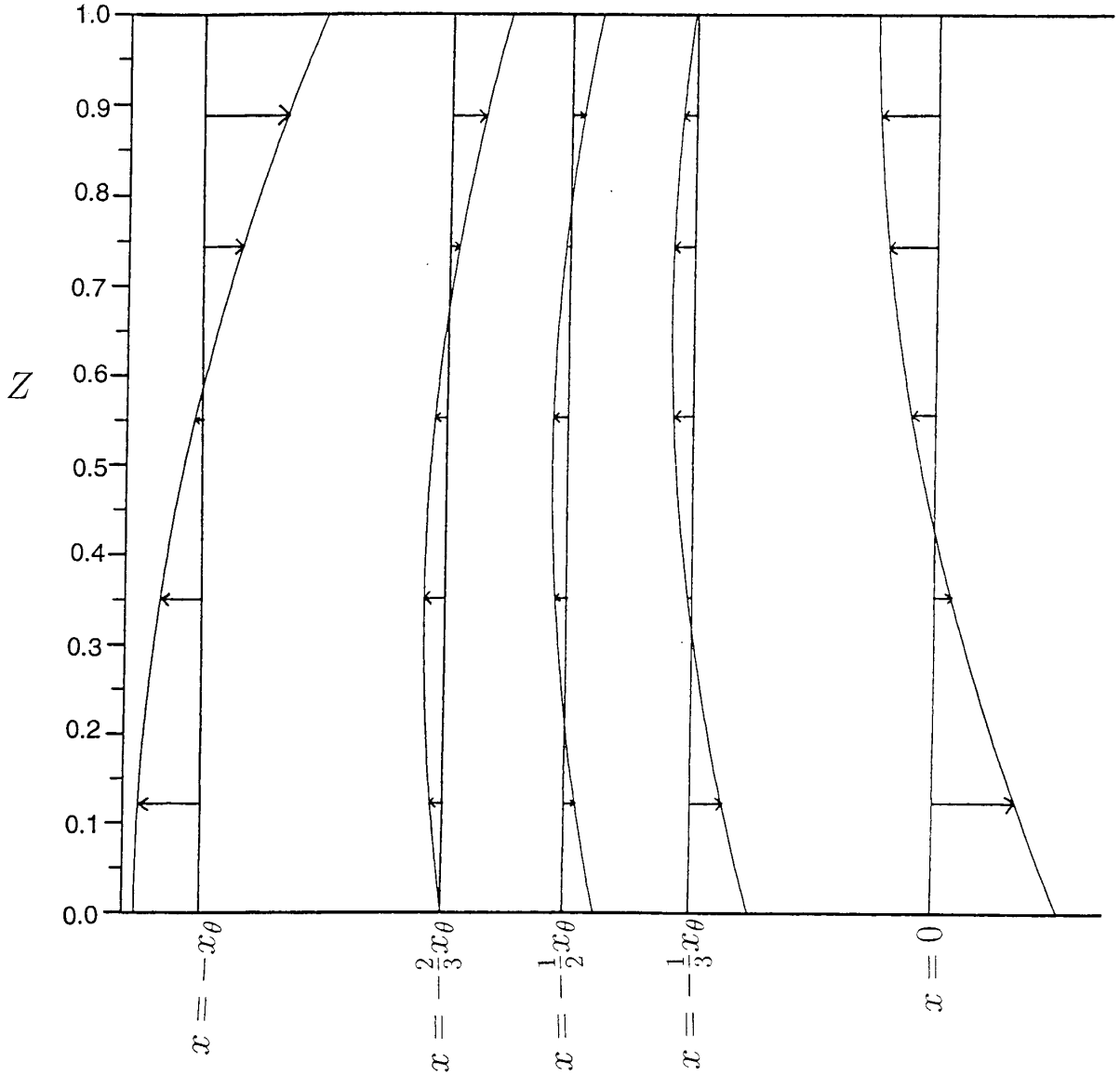
1.0
0.9
0.8
0.7
0.6
0.5
0.4
0.3
0.2
0.1
0.0
Z
$x = -x_\theta$
$x = -\frac{2}{3}x_\theta$
$x = -\frac{1}{2}x_\theta$
$x = -\frac{1}{3}x_\theta$
$x = 0$

Kay : Figure 3

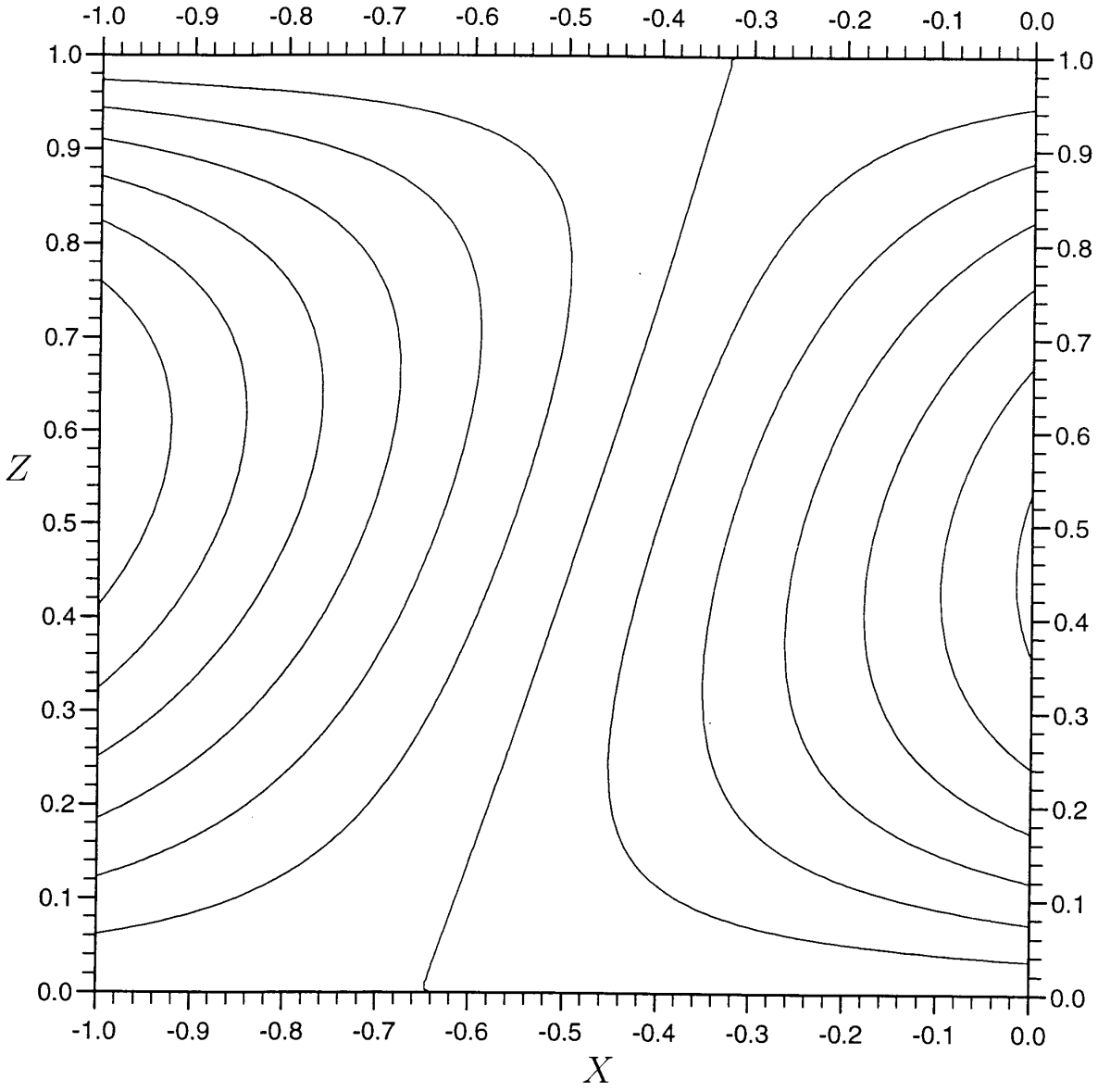

Kay : figure 4

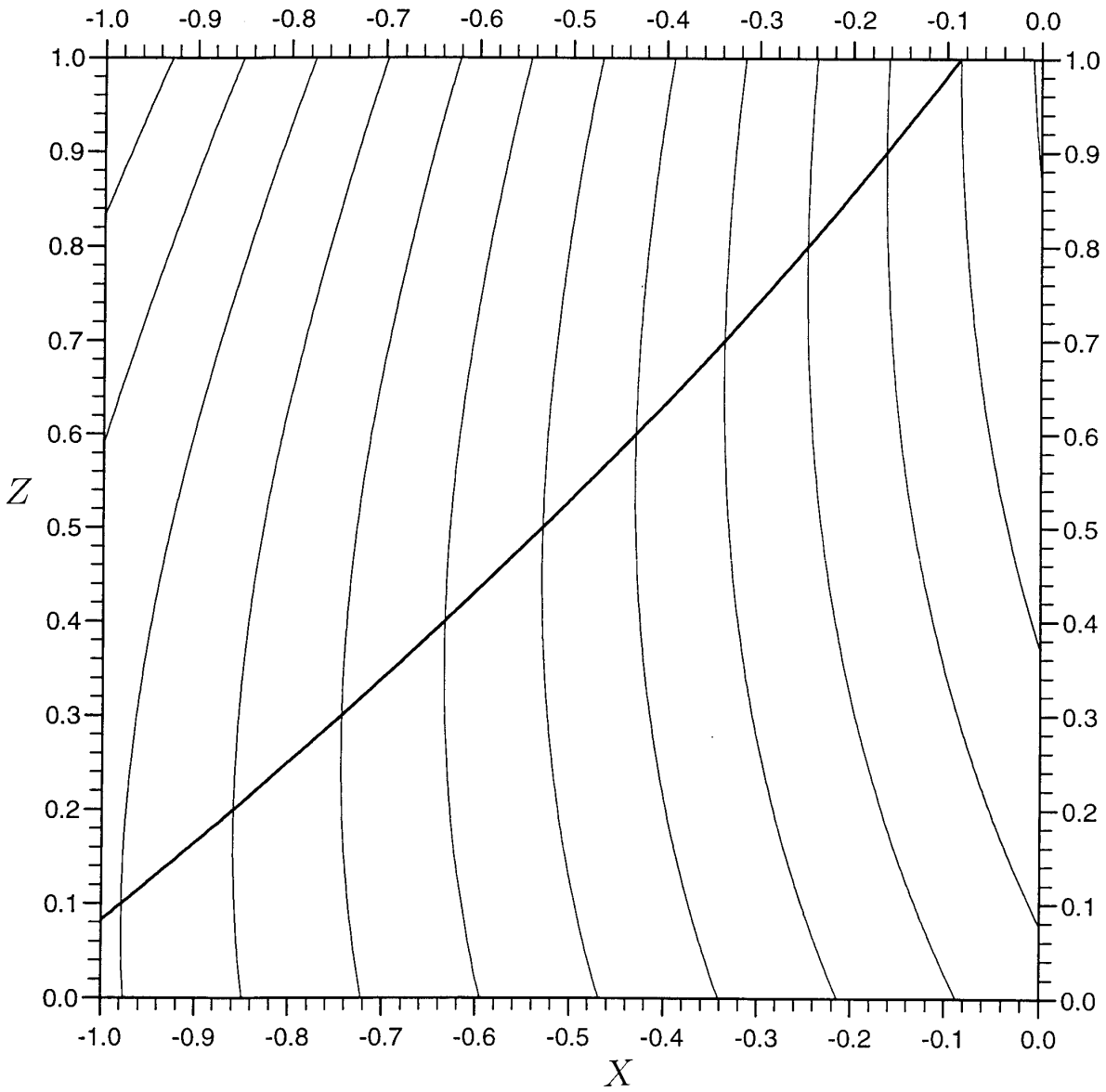

Kay : Figure 5

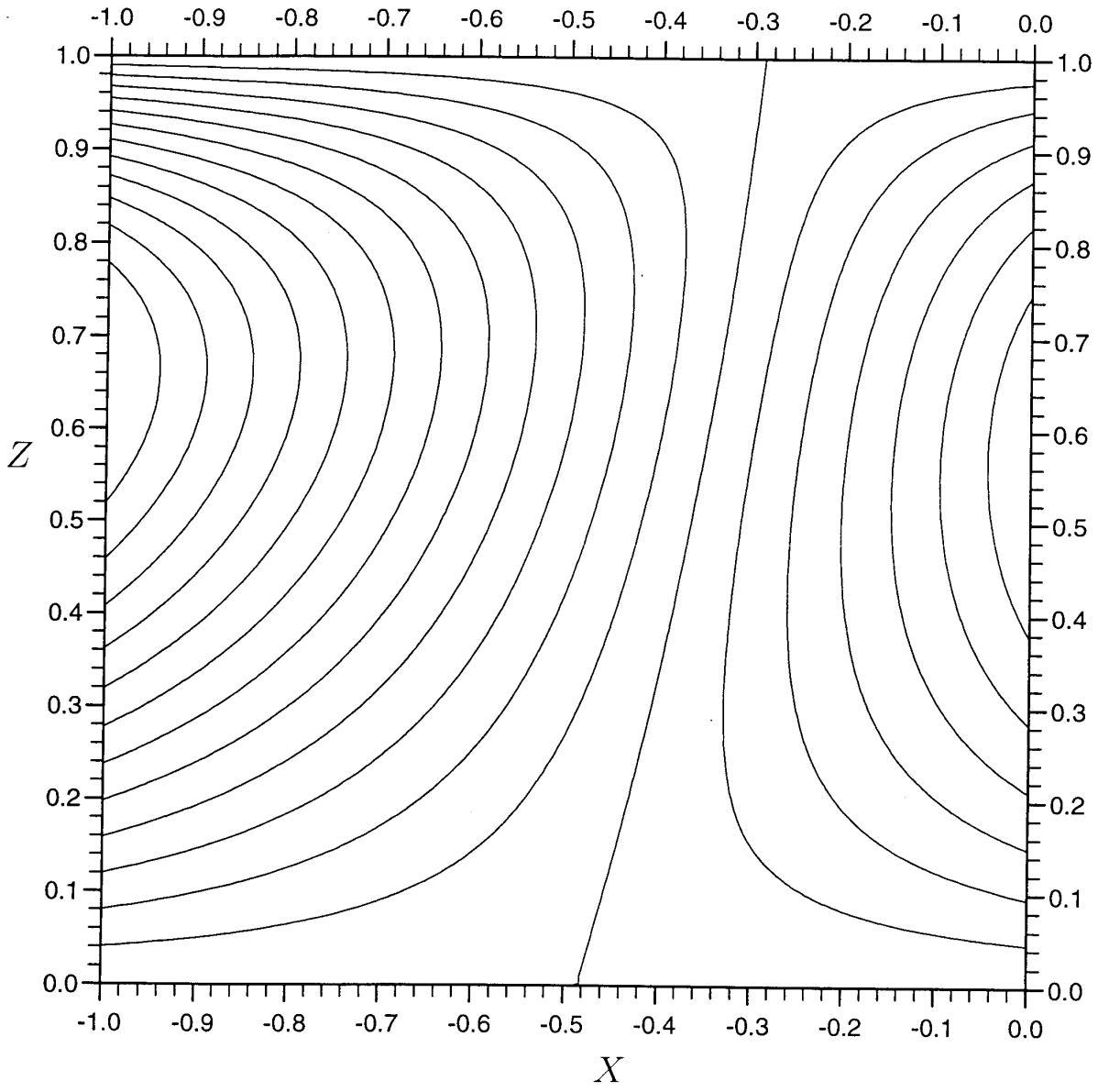

Kay : Figure 6

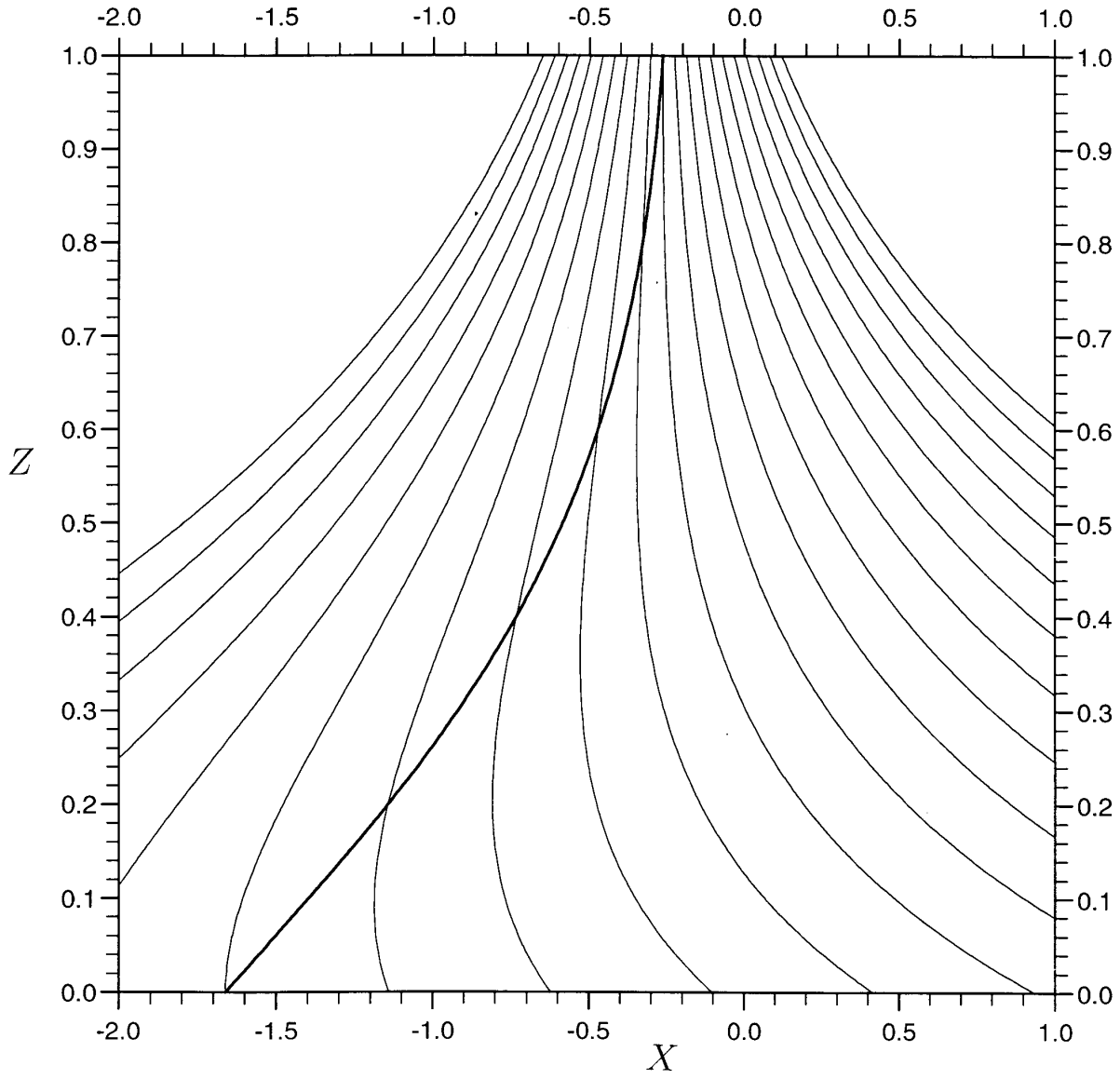

Kay: Figure 7

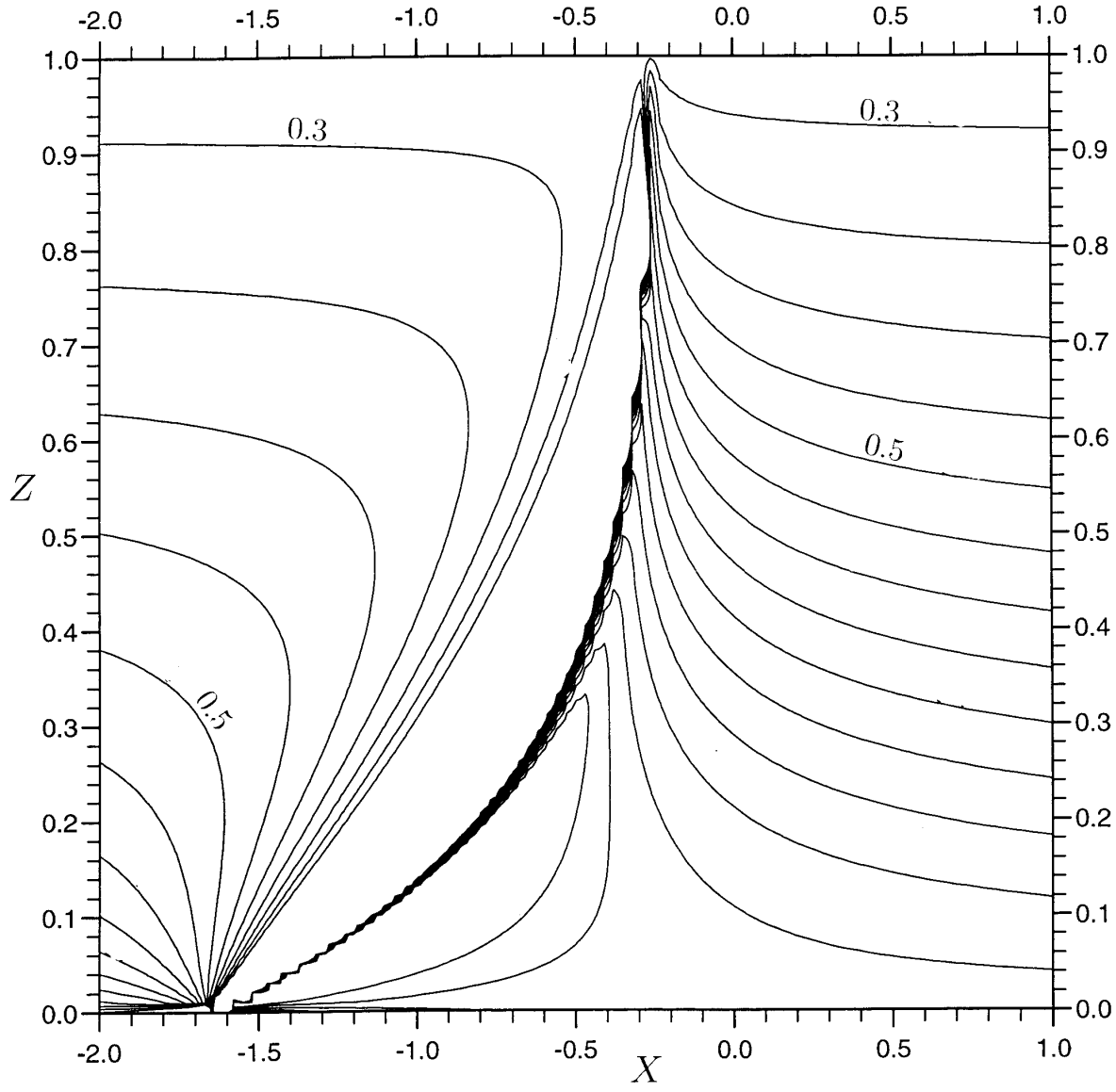

Kay : Figure 8

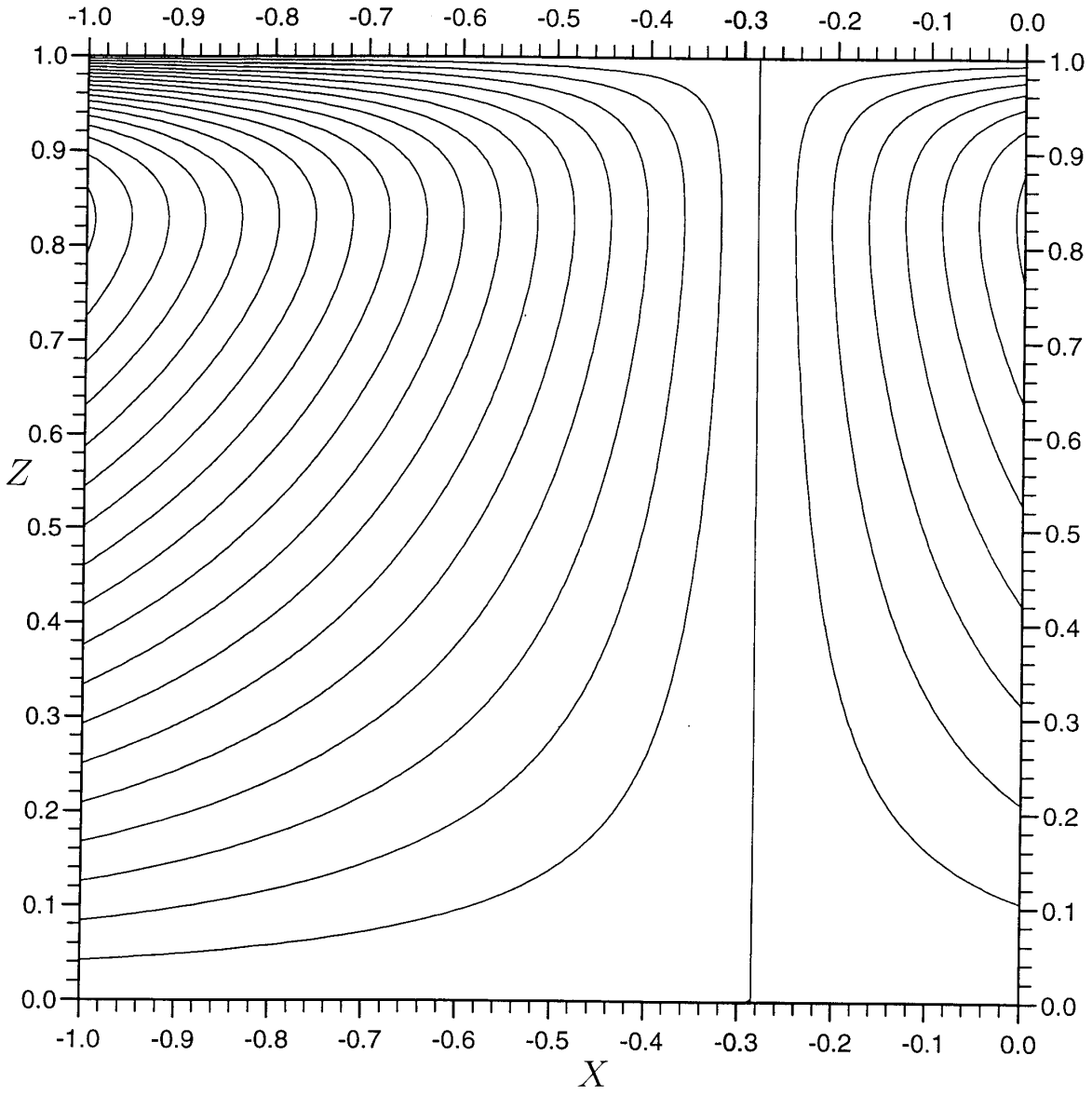

Kay : Figure 9

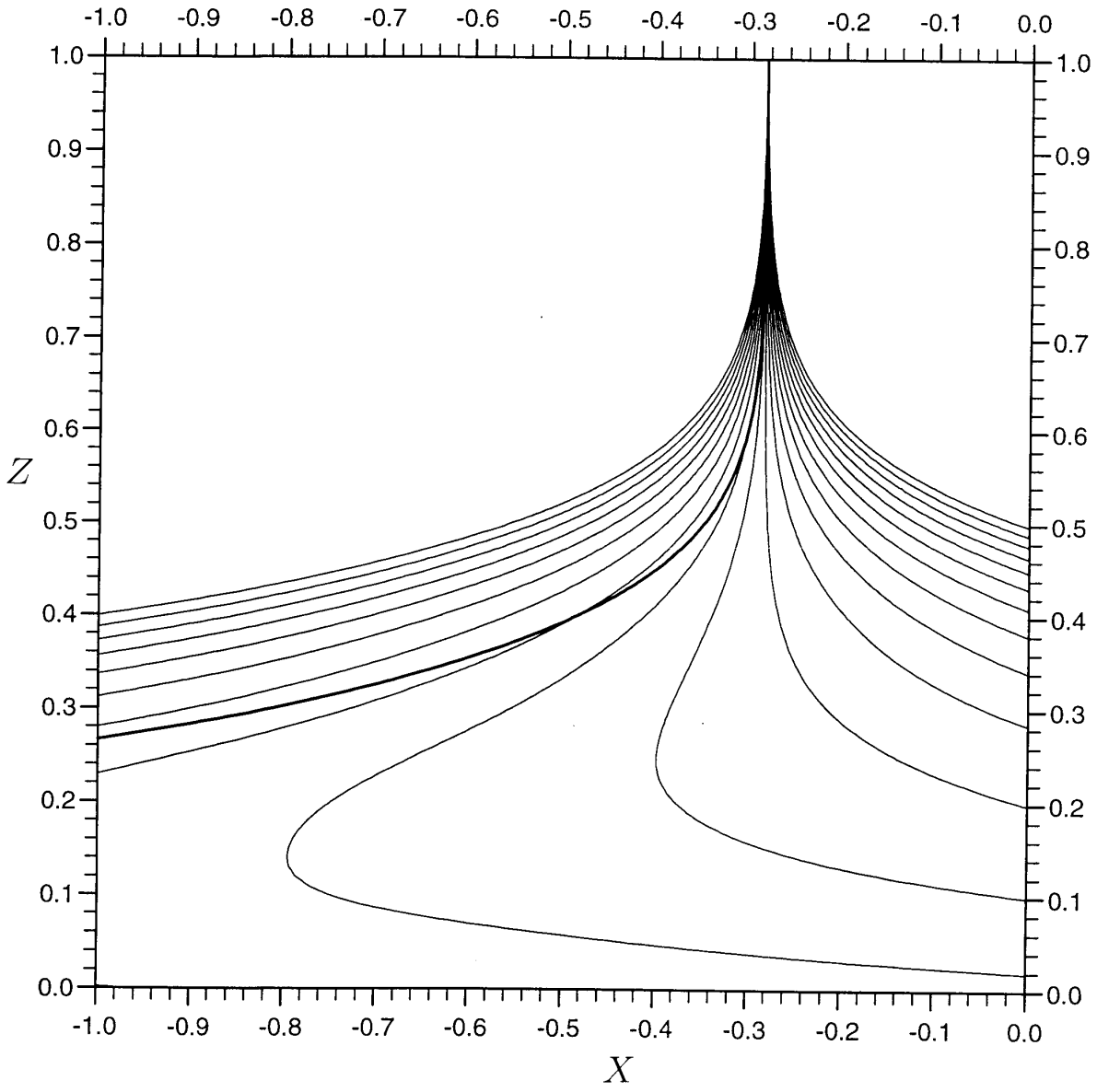

Kay : Figure 10

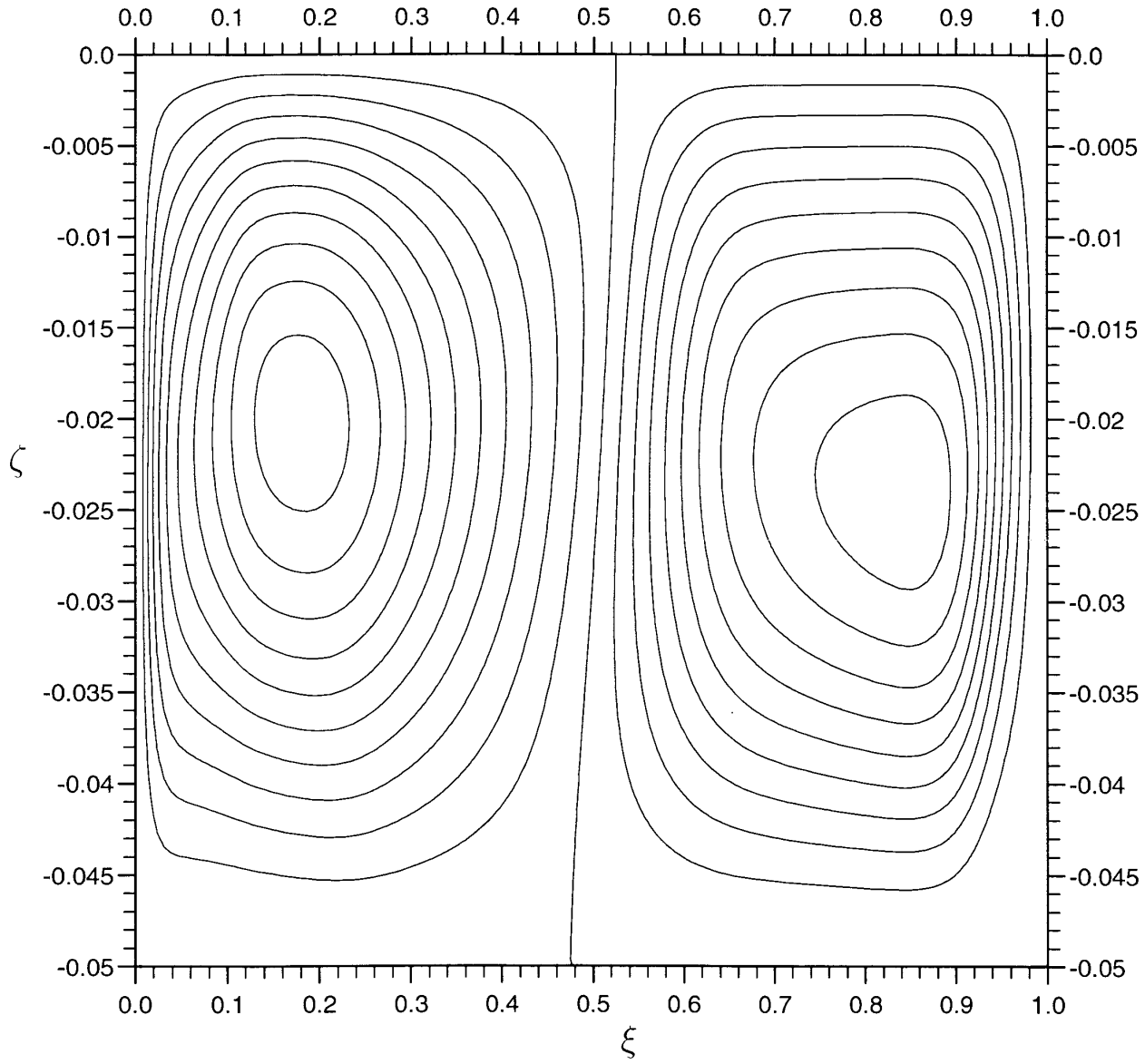

Kay: Figure 11

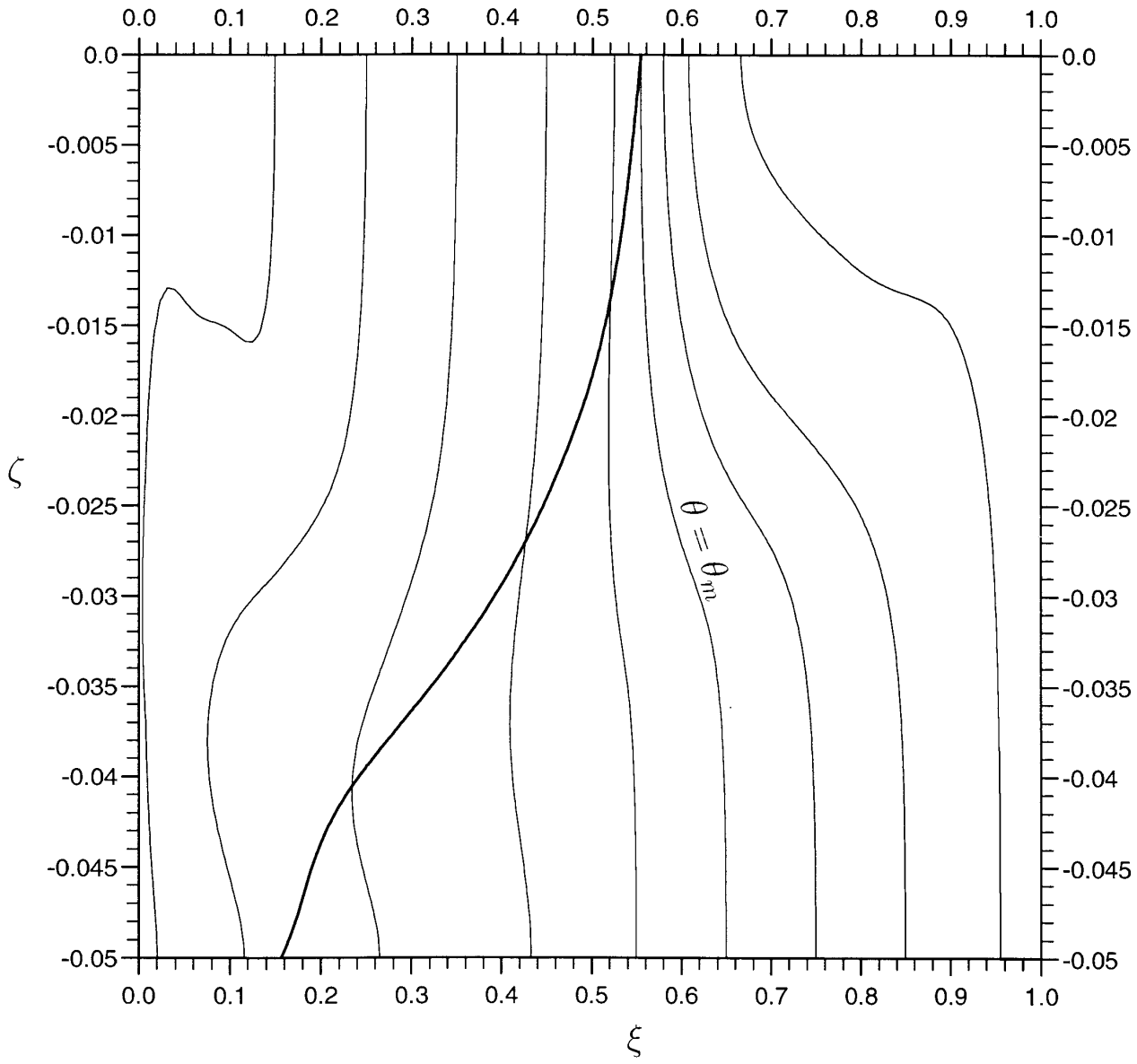

Kay: Figure 12

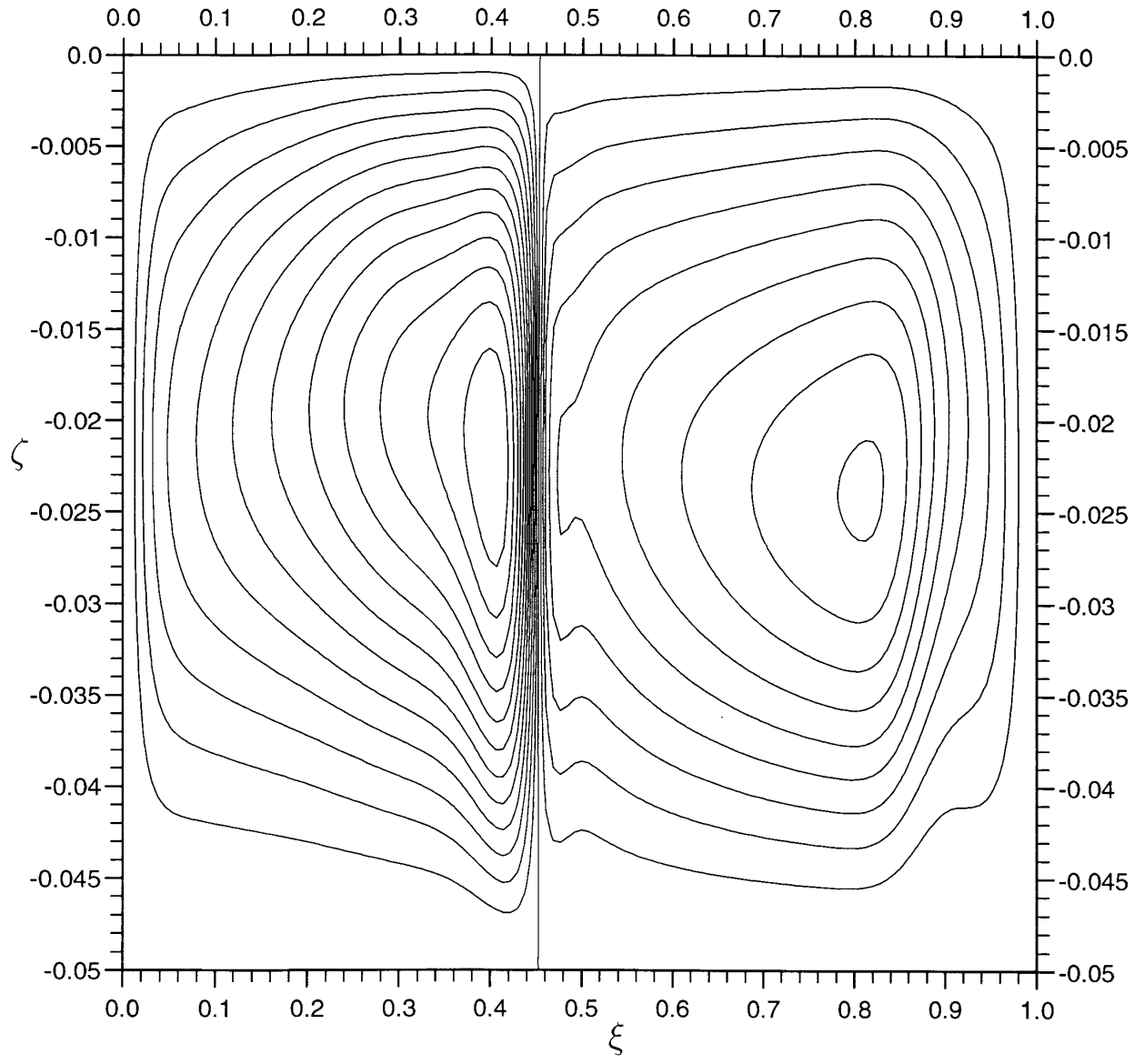

Kay : Figure 13

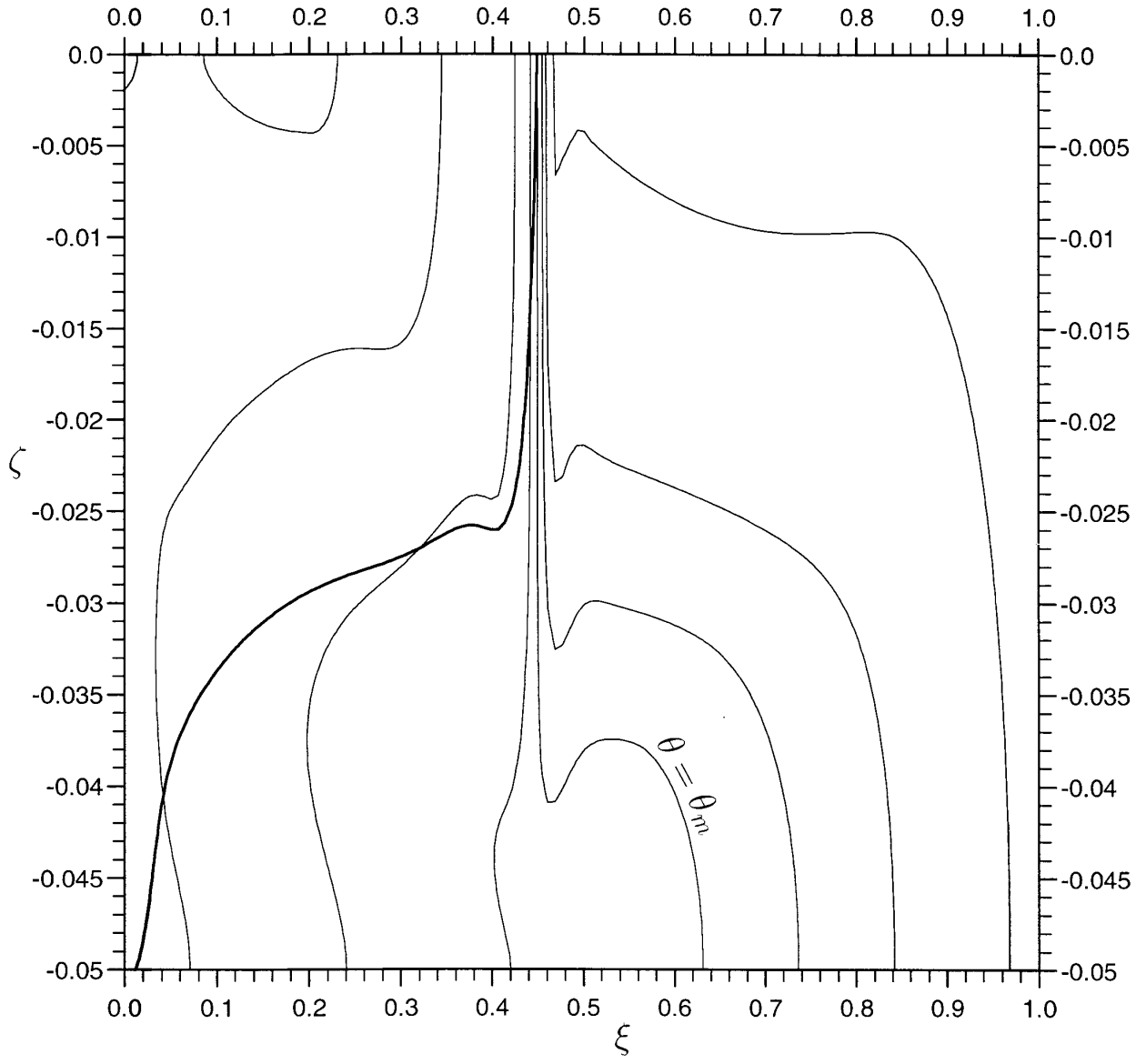

Kay: Figure 14